



Fram Strait Marine Cold Air Outbreaks in CARRA and ERA5: Effects on Surface Turbulent Heat Fluxes and the Vertical Structure of the

Downloaded from: <https://research.chalmers.se>, 2026-05-10 02:39 UTC

Citation for the original published paper (version of record):

Slättberg, N., Dahlke, S., Maturilli, M. (2025). Fram Strait Marine Cold Air Outbreaks in CARRA and ERA5: Effects on Surface Turbulent Heat Fluxes and the Vertical Structure of the Troposphere. *Journal of Geophysical Research: Atmospheres*, 130(12). <http://dx.doi.org/10.1029/2024JD042908>

N.B. When citing this work, cite the original published paper.



RESEARCH ARTICLE

10.1029/2024JD042908

Fram Strait Marine Cold Air Outbreaks in CARRA and ERA5: Effects on Surface Turbulent Heat Fluxes and the Vertical Structure of the Troposphere

Nils Slättberg^{1,2,3} , Sandro Dahlke¹ , and Marion Maturilli¹ 

¹Alfred Wegener Institute Helmholtz Centre for Polar and Marine Research, Potsdam, Germany, ²Leipzig University, Leipzig Institute for Meteorology, Leipzig, Germany, ³Chalmers Department of Space, Earth, and Environment, Chalmers University of Technology, Gothenburg, Sweden

Key Points:

- Cold and dry anomalies are present throughout most of the troposphere during Fram Strait Marine Cold Air Outbreaks
- The Fram Strait surface sensible heat flux is substantially higher in CARRA than in ERA5 while the latent heat flux is lower
- Heat flux trends around Svalbard are positive and mirror the sea ice decline while trends in ice-free Fram Strait are inconsistent

Correspondence to:

N. Slättberg,
nil.slattberg@chalmers.se

Citation:

Slättberg, N., Dahlke, S., & Maturilli, M. (2025). Fram strait marine cold air outbreaks in CARRA and ERA5: Effects on surface turbulent heat fluxes and the vertical structure of the troposphere. *Journal of Geophysical Research: Atmospheres*, 130, e2024JD042908. <https://doi.org/10.1029/2024JD042908>

Received 7 NOV 2024
Accepted 22 MAY 2025

Abstract Marine Cold Air Outbreaks (MCAOs) have a profound influence on atmospheric conditions and the surface-atmosphere heat exchange in Fram Strait and Svalbard. Comparing the global reanalysis ERA5 to its novel Arctic counterpart CARRA for November–March 1991–2020, we investigate the surface turbulent heat fluxes and the spatial characteristics associated with MCAO conditions. We find that the sensible heat flux from the surface to the atmosphere is substantially higher in CARRA while the latent heat flux is higher in ERA5. For sensible heat flux, the differences scale with the magnitude, leading to maximum disagreement over the ice-free ocean where the heat flux is high. Accounting for the varying heat flux magnitude over different surface types, we find the largest relative disagreement over sea ice. During MCAOs, negative anomalies in temperature and specific humidity are present throughout most of the troposphere in both reanalyses. Over the studied period, sea ice decline has caused positive trends in the surface-atmosphere potential temperature difference forming the basis of the MCAO index, leading to higher heat fluxes around much of Svalbard. In ice-free Fram Strait however, both reanalyses show negative trends in the MCAO index and the heat fluxes in January, when the increase in potential temperature is larger at 850 hPa than at the surface. Finally, large differences between two individual MCAO cases are found in reanalysis heat flux variability and radiosonde-derived atmospheric conditions over Svalbard.

Plain Language Summary In Fram Strait, located between Greenland and Svalbard, Marine Cold Air Outbreaks (MCAOs) are formed when cold air moves from sea ice covered regions out over the open ocean. Because the air is so cold and dry compared with the ocean, vigorous heat transfer occurs in the form of sensible heat flux (heat from the ocean surface is transported to the air) and latent heat flux (water is evaporated). We compare the reanalysis data sets ERA5 and CARRA, and find that the sensible heat flux is much higher in CARRA while the latent heat flux is higher in ERA5. We also find that during MCAO conditions, almost the entire troposphere (approximately the lowest 10 km of the atmosphere) becomes colder and drier. Over the studied period, sea ice has decreased in much of the region, and therefore the heat fluxes have increased. In January in ice-free Fram Strait however, the atmosphere warmed faster than the ocean surface, causing a smaller temperature difference between the surface and the air. Therefore, the heat fluxes in January have decreased there. Finally, we compare two MCAO cases demonstrating large differences in the heat fluxes as well as atmospheric conditions measured by radiosondes launched in Svalbard.

1. Introduction

The Arctic climate and environment is transforming and particularly rapid changes are seen in the winter conditions of the Svalbard and Fram Strait region (e.g., Dahlke & Maturilli, 2017; López-Moreno et al., 2016; Maturilli & Kayser, 2017; Urbański & Litwicka, 2022). In Fram Strait (Figure 1), the West Spitsbergen Current (WSC) brings warm water northwards while the East Greenland Current carries cold Arctic water southwards (Rudels et al., 2012). Significant meridional transport occurs in the atmosphere as well, as cyclones (Aue et al., 2022; Brümmer et al., 2001) and related intrusions of warm, moist air enters the Arctic from lower latitudes (Fearon et al., 2021). In the opposite direction, cold and dry Arctic air masses are advected in surges known as Marine Cold Air Outbreaks (MCAOs), which are common in Fram Strait during winter (Brümmer, 1997; Dahlke et al., 2022; Papritz et al., 2019; Papritz & Spengler, 2017). Consequently, this region represents a major gateway of atmospheric (Tsukernik et al., 2007) and oceanic (Aagaard & Greisman, 1975)

© 2025. The Author(s).

This is an open access article under the terms of the [Creative Commons Attribution License](https://creativecommons.org/licenses/by/4.0/), which permits use, distribution and reproduction in any medium, provided the original work is properly cited.

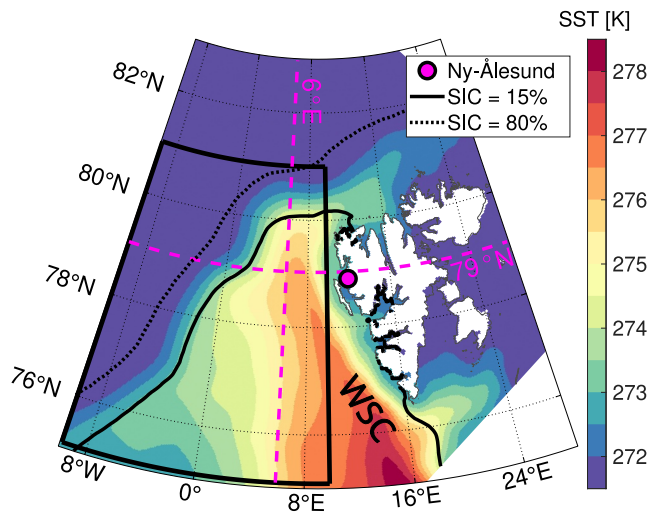


Figure 1. The study area: Fram Strait and Svalbard. CARRA extended winter (November–March) mean sea surface temperature 1991–2020 is shown by the colormap, with the warm tongue in eastern Fram Strait indicating the presence of the West Spitsbergen Current (WSC). The region for which the MCAO index and spatially averaged variables were calculated is marked by the black box (referred to as the “Fram Strait box,” see Section 3.1). The cross sections at 6°E and 79°N, respectively, are marked by pink dashed lines, and the location of the radiosonde launch site in Ny-Ålesund is marked by a pink dot. Contours mark the ice edge (CARRA extended winter mean sea ice concentration (SIC) = 15%) and the transition from the marginal ice zone to sea ice (SIC = 80%).

energy transports between the Arctic and lower latitudes, making it a hot-spot for ocean–atmosphere energy exchanges (Papritz & Spengler, 2017; Wickström et al., 2020). Such exchanges include the turbulent heat fluxes, that is, surface sensible heat flux (SSHF) and surface latent heat flux (SLHF). These fluxes (collectively termed “heat fluxes” throughout this paper) exert a growing influence on Arctic climate variability as the temperature difference between the surface and the lower atmosphere changes in response to trends in sea ice characteristics (Taylor et al., 2018).

MCAOs are known to favor large heat fluxes in the Arctic (Papritz & Spengler, 2017). As cold air masses are advected over the relatively warm ocean surface they pick up heat and moisture, which leads to a rapid transformation of the air mass and can result in vigorous convection (Pithan et al., 2018). At the same time, the heat transfer cools the ocean mixed layer, facilitating dense water formation (Papritz & Spengler, 2017). In fact, MCAOs account for as much as 60%–80% of the oceanic wintertime heat loss in the Nordic and Irminger Seas (Papritz & Spengler, 2017). MCAOs are thus of great importance for the transfer and distribution of heat within the highly coupled Arctic climate system.

As for longer-term MCAO changes, Dahlke et al. (2022) used data from the ERA5 reanalysis to calculate a Fram Strait MCAO index based on the surface–atmosphere temperature difference and investigate its trends over the 1979–2020 period. For December and January, Dahlke et al. (2022) observed negative MCAO index trends, which were attributed to the lower atmosphere warming more quickly than the ocean surface. For March, in contrast, Dahlke et al. (2022) identified a positive MCAO index trend, which was related to increased northerlies across Fram Strait. The identification of significant MCAO index trends in the Fram Strait prompts the question of whether the heat fluxes are adjusting in response.

As noted above, MCAOs initiate convection, altering the vertical structure of the originally cold and dry air mass. MCAOs are thus associated with low static stability in the near-surface air masses and typically result in organized convection, as often revealed by the formation of cloud streets or cellular cloud patterns (Brümmer & Pohlmann, 2000; Kolstad, 2011). Moreover, they often bring about severe weather and conditions suitable for the formation of intense mesoscale cyclones (Terpstra et al., 2021) such as polar lows (Kolstad, 2011). Airborne campaigns have allowed observations of the lower troposphere during specific MCAO cases (e.g., Hartmann et al. (1997); Knudsen et al. (2018); Michaelis et al. (2022); Kirbus et al. (2024)). In addition, Meyer et al. (2021) used a novel approach to investigate the 3-D structure of MCAO cases in the Barents and Nordic seas in ERA5. They point out that there is considerable variation in the shape and dynamics of different MCAOs. Therefore, we examine atmospheric properties and heat fluxes associated with MCAO conditions on a climatological time scale. For this purpose, we use data from the global atmospheric reanalysis ERA5 (Hersbach et al., 2017, 2018, 2020) and its regional counterpart, the Copernicus Arctic Regional ReAnalysis (CARRA; Schyberg et al., 2020a, 2020b). In addition, we provide detailed examination of two separate MCAO cases, for which we include radiosonde data from Ny-Ålesund, Svalbard.

Focusing on the Svalbard and Fram Strait region in November–March, when the prevalence of MCAOs is high, and limiting our study to 1991–2020, we investigate the following:

1. How does the novel CARRA reanalysis compare with ERA5 in terms of representing the heat fluxes and their relation with Fram Strait MCAOs?
2. What characterizes the vertical structure of the atmosphere during MCAO conditions and how does it vary over different surfaces and between CARRA and ERA5?
3. What are the CARRA and ERA5 wintertime trends in the MCAO indices and heat fluxes?

2. Data

We use the ERA5 and CARRA reanalyses for our climatological analysis. For our two MCAO case studies, we also use data from radiosondes (Maturilli, 2008, 2020) launched in Ny-Ålesund, which is located on the west-coast of Svalbard (Figure 1). Radiosondes are launched from Ny-Ålesund daily at 12 UTC, with additional launches during specific campaigns, enabling analysis at a higher temporal resolution. The case studies are focused on two periods in January 2007 and March 2020, when radiosondes were launched one to two times per day (12 and 18 UTC) and four times per day (00, 06, 12, and 18 UTC), respectively.

Reanalysis assimilates observations into numerical weather prediction models to produce a physically consistent gridded data set. Unlike in situ observations and satellite data, reanalysis provides the means to study spatio-temporal variability over several decades. ERA5 has been evaluated in a comparison focused on the Fram Strait region, and was found to perform better than other reanalyses (Graham et al., 2019). It has a horizontal resolution of 0.25° (ca 31 km) and is produced by the European Centre for Medium-range Weather Forecasts (ECMWF) within the Copernicus Climate Change Service, Integrated Forecasting System (IFS) Cy41r2.

CARRA is a regional Arctic reanalysis receiving its boundary conditions from ERA5 (Bengtsson et al., 2017; Køltzow et al., 2022). Data are produced for two spatial domains in the North Atlantic sector of the Arctic. We use data from the western domain since it better covers the Fram Strait. CARRA is based on the HARMONIE-AROME numerical weather prediction system cycle 40h1.1 with the surface physics module SURFEX v7.3 (Le Moigne, 2013; Masson et al., 2013). Compared with ERA5, the horizontal resolution is higher (2.5 km), more local observations are assimilated, and the treatment of cold surfaces is improved (Køltzow et al., 2022; Yang et al., 2020). In an evaluation focusing on 2 m air temperature and 10 m wind speed (WS10), Køltzow et al. (2022) found that CARRA agrees better than ERA5 with observations. Recently, Kirbus et al. (2024) provided a first evaluation and comparison of ERA5 and CARRA during an MCAO in Fram Strait. They found that biases in the boundary layer temperature over sea ice and specific humidity over ocean were smaller in CARRA than in ERA5.

We base our analysis of CARRA and ERA5 on single level variables as well as pressure level data from 1,000 hPa to 300 hPa. CARRA has 14 pressure levels in this range and ERA5 has 20. The data are downloaded on the highest temporal resolution (hourly for ERA5 and 3-hourly for CARRA) and averaged into daily means. Following the recommendation in the user guide (Nielsen et al., 2022), we removed the spin-up period (first 6 hr of each run) from the CARRA heat fluxes.

The turbulent heat fluxes in CARRA and ERA5 are based on bulk aerodynamic formulas. Such formulas, described by for example Pond et al. (1974), can generally be written as

$$\text{SSHf} = \rho c_p C_H U (T_s - T_a) \quad (1)$$

$$\text{SLHF} = \rho L_v C_Q U (q_s - q_a) \quad (2)$$

where ρ is air density, c_p is the specific heat of air, C_H is a heat transfer coefficient, U is wind speed, L_v is the latent heat of vaporization, and C_Q is a moisture transfer coefficient. $T_s - T_a$ and $q_s - q_a$ represents the temperature and specific humidity gradients between the surface (s) and the overlying atmosphere (a). The potential temperature is used in the expression $T_s - T_a$ for CARRA (Le Moigne, 2013) while dry static energy is used in ERA5 (ECMWF, 2016). As for the humidity gradient, q_s is the saturation specific humidity at surface temperature. In CARRA, the heat transfer coefficient C_H is derived from the Richardson number using the parameterization from Louis (1979), and $C_Q = C_H$ (Le Moigne, 2013). In the case of ERA5, the calculation of C_H and C_Q requires the Obhukov length, which is retrieved using an iterative process relating the stability parameter to the bulk Richardson number (ECMWF, 2016). Roughness lengths for momentum (z_{0M}), heat (z_{0H}), and moisture (z_{0Q}) are also needed to calculate C_H and C_Q (Table 1). In CARRA over sea ice, $z_{0M} = 3 \times 10^{-3}$ m and $z_{0Q} = z_{0H} = 3 \times 10^{-4}$ m (Yang et al., 2020). Over ice-free sea, the roughness lengths are based on Charnock's relation, that is, $z_{0Q} = z_{0H} = z_{0M} = \alpha \frac{u_*^2}{g}$ m, where α is the Charnock parameter (set to 0.015), u_* is the friction velocity and g is the gravitational acceleration (Charnock, 1955; Le Moigne, 2013). In ERA5 over sea ice, z_{0M} depends on the sea ice concentration (SIC) while $z_{0Q} = z_{0H} = 10^{-3}$ m (ECMWF, 2016). Unlike CARRA, ERA5 lacks a parameterization of a snow layer on top of the sea-ice (Batak & Müller, 2019). As for the ERA5

Table 1
Roughness Length Summary Table

	OCEAN		SEA ICE	
	CARRA	ERA5	CARRA	ERA5
z_{0M} (m)	$0.015 \frac{u_*^2}{g}$	$0.11 \frac{\nu}{u_*} + \alpha \frac{u_*^2}{g}$	3×10^{-3}	$\geq 10^{-3}$
z_{0H} (m)	$0.015 \frac{u_*^2}{g}$	$0.4 \frac{\nu}{u_*}$	3×10^{-4}	10^{-3}
z_{0Q} (m)	$0.015 \frac{u_*^2}{g}$	$0.62 \frac{\nu}{u_*}$	3×10^{-4}	10^{-3}

Note. See Section 2 for details.

roughness lengths over ice-free sea, $z_{0M} = 0.11 \frac{\nu}{u_*} + \alpha \frac{u_*^2}{g}$ m, where ν is the kinematic viscosity and the Charnock parameter α is provided by the wave model in IFS. The Charnock relation is thereby utilized, but unlike CARRA, there is an additional term to account for low wind speeds, during which the sea surface becomes aerodynamically smooth and the roughness length scales with ν rather than g . The heat and moisture roughness lengths over ice-free sea are calculated as $z_{0H} = 0.4 \frac{\nu}{u_*}$ m and $z_{0Q} = 0.62 \frac{\nu}{u_*}$ m (Beljaars, 1995; Brutsaert, 1982; ECMWF, 2016).

3. Methods

3.1. MCAO Index

Since MCAOs have a typical lifetime of days (Terpstra et al., 2021), we used daily mean data to calculate the Fram Strait MCAO indices for CARRA and ERA5 over the investigated period (November–March 1991–2020). MCAOs are characterized by large vertical potential temperature differences between the warmer ocean surface and the colder lower troposphere. Following for example, Papritz et al. (2015), Kolstad (2017), Knudsen et al. (2018), Dahlke et al. (2022), and Walbröl et al. (2024), we therefore used the difference between potential skin temperature (θ_s) and potential air temperature at the 850 hPa level (θ_{850}) as a proxy for MCAOs. Different studies have used other levels for the air temperature, for example, 700 hPa (Kolstad & Bracegirdle, 2008) or 800 hPa (Fletcher et al., 2016), but we chose 850 hPa since it is closely related to the heat fluxes (Papritz et al., 2015). The calculation was applied to the region 10°W–10°E, 75°N–81°N, which we refer to as the “Fram Strait box” (black box in Figure 1). Only the ice-free (daily mean SIC < 15%) part of the Fram Strait box was considered. The potential temperature difference was thus calculated for every daily mean timestep t with SIC < 15% and every grid point s with SIC < 15% as

$$\theta_s - \theta_{850} = \theta_s(t, s) - \theta_{850}(t, s). \quad (3)$$

The potential temperature difference was then spatially averaged over the Fram Strait box to obtain the MCAO index. For our two case studies, we used 3-hourly data instead of daily to be able to explore the temporal evolution during two individual MCAOs.

3.2. Statistical Methods and Data Treatment

We used linear regression for computing trends over time and relationships between variables, and Pearson's R for correlation, in both cases with 95% as confidence level. In addition, we calculated the difference between the heat fluxes in CARRA and ERA5 as the Root Mean Squared Error (RMSE) over three different surface categories: ice-free ocean, the marginal ice zone (MIZ), and sea ice. The surface categories are determined using daily mean SIC and defining ice-free ocean as SIC < 15%, MIZ as SIC = 15%–80%, and sea ice as SIC > 80% (Strong et al., 2017). We thereafter normalized the RMSE by the interquartile range (IQR) of the heat flux in CARRA. Thereby, we express the RMSE as a percentage of the IQR of the CARRA SSHF and SLHF, respectively, over each respective surface category s :

$$\text{Normalized RMSE}_s = 100 \left(\frac{\text{RMSE}_s}{\text{IQR}_s} \right) \quad (4)$$

The objective of relating the RMSE to the magnitude of the heat flux is to make the RMSEs somewhat comparable despite the large difference in heat flux magnitude over the different surfaces. Throughout this paper, positive values denote a heat flux from the surface to the atmosphere.

3.3. MCAO Threshold and Composite Analysis

MCAOs are often classified using one or several threshold values of the MCAO index. Since the Fram Strait region is prone to strong MCAOs (Papritz & Spengler, 2017), we chose 8 K, which is classified as strong MCAO in Dahlke et al. (2022) and Walbröl et al. (2024). This threshold corresponds to the 81st (83rd) percentile of the daily mean MCAO index for CARRA (ERA5), and ensures that a sufficient number of observations (at least 96

(91) in CARRA (ERA5)) are included in the composite for each month. Applying a different threshold yielded similar spatial patterns in the winter mean MCAO anomalies, although the magnitude was different (Figure A1). Composites showing the mean conditions were computed as the mean of a meteorological variable x for all days in month m . Similarly, the MCAO composites are the mean of x for all days in month m with the MCAO index > 8 K. The monthly composites were then averaged to produce a mean for the entire extended winter, and the MCAO anomalies were computed from these averaged composites as $x_{MCAO} - x_{mean}$. Composites were computed for surface variables as well as the atmospheric cross sections described below.

3.4. Atmospheric Cross Sections

To investigate the vertical structure of the troposphere during MCAOs, we extracted a meridional cross section at 6°E from 75°N to 83°N , and a zonal cross section at 79°N from 10°W to 26°E . The former exclusively covers sea ice and ocean, while the latter also encompasses Svalbard land regions, including Ny-Ålesund, the radiosonde launch site for the case studies. Data on pressure levels with higher pressure than the surface were removed to avoid presenting data for non-existing pressure levels. To analyze the CARRA-ERA5 differences, we linearly interpolated the cross sections to the same axes using the nearest two grid points and subtracted the ERA5 data from the CARRA data. Since CARRA (ERA5) has a lower vertical (horizontal) resolution, the CARRA cross sections were interpolated to the vertical levels of ERA5, and the ERA5 cross sections to the horizontal coordinates of CARRA.

4. Results

4.1. Fram Strait MCAO Indices and Heat Fluxes in CARRA and ERA5

To be able to compare their interannual variability and evolution over the 1991–2020 period, we calculated monthly mean time series of the CARRA and ERA5 MCAO indices and surface heat fluxes for the ice-free fraction of the Fram Strait box. Since Fram Strait MCAO index trends have previously been found to vary between months (Dahlke et al., 2022), we compute the trends for each individual month rather than the winter mean. The monthly mean CARRA and ERA5 MCAO indices have similar temporal variability, but the MCAO index is slightly higher in CARRA (mean = 2.8 K) than in ERA5 (mean = 2.5 K), with larger differences in the first half of the period (Figure 2). Similar to Dahlke et al. (2022), the MCAO index trends are negative in winter and positive in March. However, the trends lack statistical significance, except for the negative January trend in CARRA and the positive March trend in ERA5. For the surface heat fluxes, the interannual variability and the direction of the trends is similar to the MCAO indices, highlighting the strong impact of MCAO variability on the heat fluxes. Although the temporal variability is similar in CARRA and ERA5, the heat flux magnitudes differ substantially between the two reanalyses, as we investigate further below. Specifically, the SSHF is larger in CARRA, especially during the first half of the period, while the SLHF is larger in ERA5.

We compare CARRA-ERA5 differences in daily mean heat fluxes over ice-free ocean, the MIZ and sea ice, for non-MCAO days (CARRA MCAO index ≤ 0 K; Figures 3a and 3b) and strong MCAO days (CARRA MCAO index > 8 K; Figures 3c and 3d). The CARRA-ERA5 SSHF disagreement increases with the SSHF, and is therefore largest over ice-free ocean during MCAOs, when the largest differences exceed 300 Wm^{-2} (Figure 3c). In terms of normalized differences (see Section 3.2), the non-MCAO SSHF differ by 32%, 42%, and 60% of the CARRA SSHF IQR over ocean, MIZ and sea ice, respectively. For the MCAO fluxes, the corresponding normalized RMSEs are 44%, 41%, and 61%. The SLHF is consistently larger in ERA5, especially during MCAOs (Figure 3d). The normalized RMSEs are 33%, 58%, and 132% for non-MCAOs and 44%, 82%, and 263% for MCAOs. Thus, while the largest absolute differences between CARRA and ERA5 are found in SSHF over the ocean, the normalized difference is largest over ice, and is particularly large for SLHF during MCAOs. Overall, the CARRA-ERA5 heat flux differences in Figure 3 are similar to the differences during March and April MCAOs reported by Kirbus et al. (2024). However, here we show that the CARRA-ERA5 heat flux differences are present also in winter and during non-MCAO conditions.

In the following, we investigate the relative influences of the daily mean MCAO index and WS10 on the heat fluxes in the ice-free Fram Strait box. For both heat fluxes, the correlation with WS10 is lower than the correlation with the MCAO index. The latter shows explained variances (R^2) of at least 0.62 in both reanalyses, indicating that at least 62% of the variability in the heat fluxes can be explained by the MCAO index (Table 2). Moreover, the

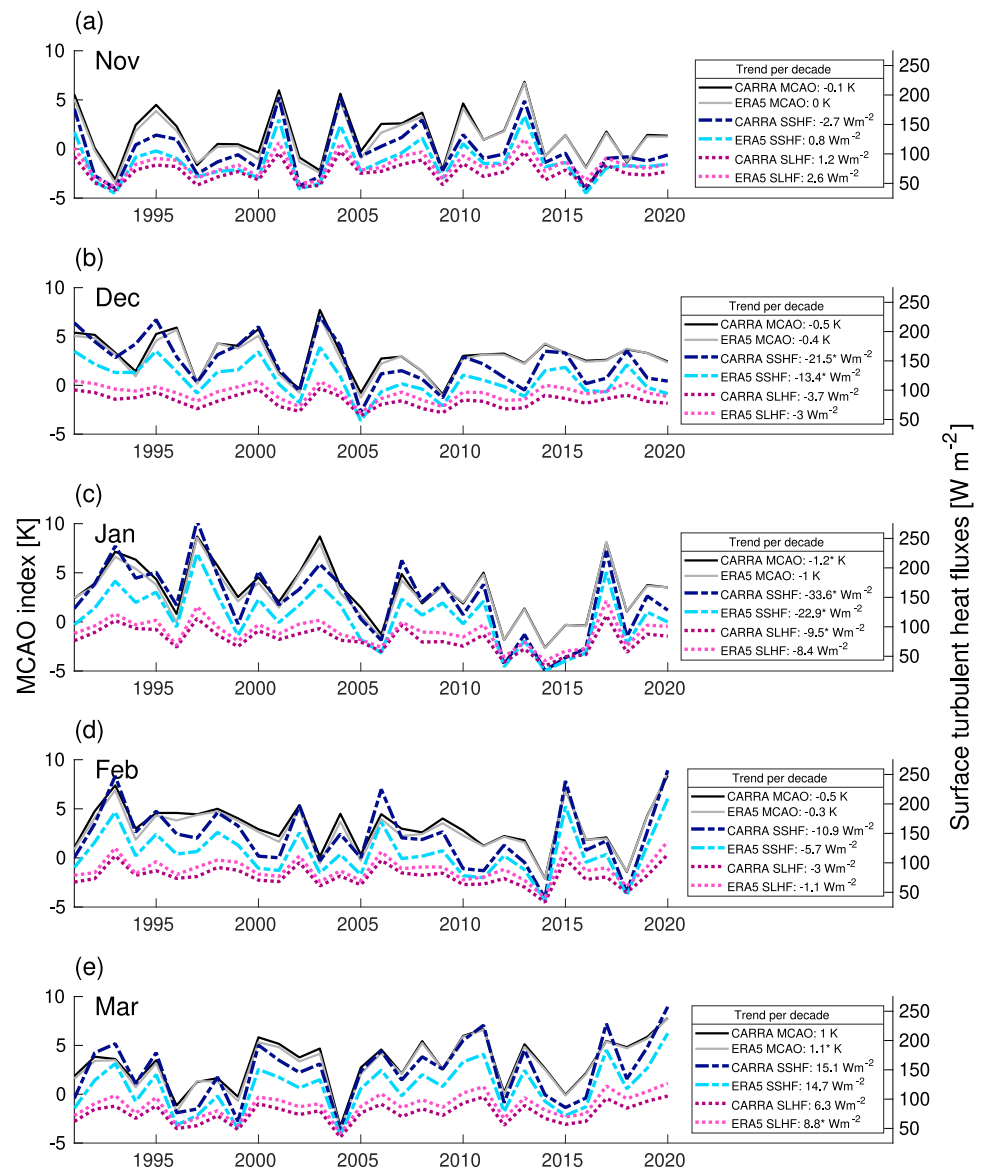


Figure 2. Monthly mean 1991–2020 MCAO indices for CARRA (black, left y-axis) and ERA5 (gray, left y-axis) are plotted along with surface sensible heat flux (SSHF; dash-dot, right y-axis) and surface latent heat flux (SLHF; dotted, right y-axis), for November to March (a–e). The decadal trends are given in the box to the right in each subplot, where a star denotes statistical significance at the 95% confidence level. All data were averaged over the ice-free part of the Fram Strait box (black box in Figure 1).

normalized regression coefficients indicate that MCAO index variability has a larger impact than WS10 on the heat fluxes. This is in line with Taylor et al. (2018), who tested the sensitivities of satellite-derived heat fluxes to wind speed and the vertical temperature and humidity gradients between the surface and the atmosphere. They found that SSHF (SLHF) variability is dominated by the vertical temperature (humidity) gradient while wind speed plays a smaller role.

The heat fluxes are plotted against WS10 for different MCAO index classes in Figure 4. During strong MCAOs (MCAO index > 8 K), the minimum SSHF occurs with WS10 below 3 ms^{-1} and lies around 80 Wm^{-2} in both reanalyses. The very highest SSHF only occurs with WS10 above 15 ms^{-1} . As seen also in the previous figure, these SSHF differ greatly between the reanalyses, with CARRA reaching 1014 Wm^{-2} (Figure 4a) and ERA5 615 Wm^{-2} (Figure 4c). The minimum SLHF lies around 50 Wm^{-2} in CARRA (Figure 4b) and 60 Wm^{-2} in ERA5

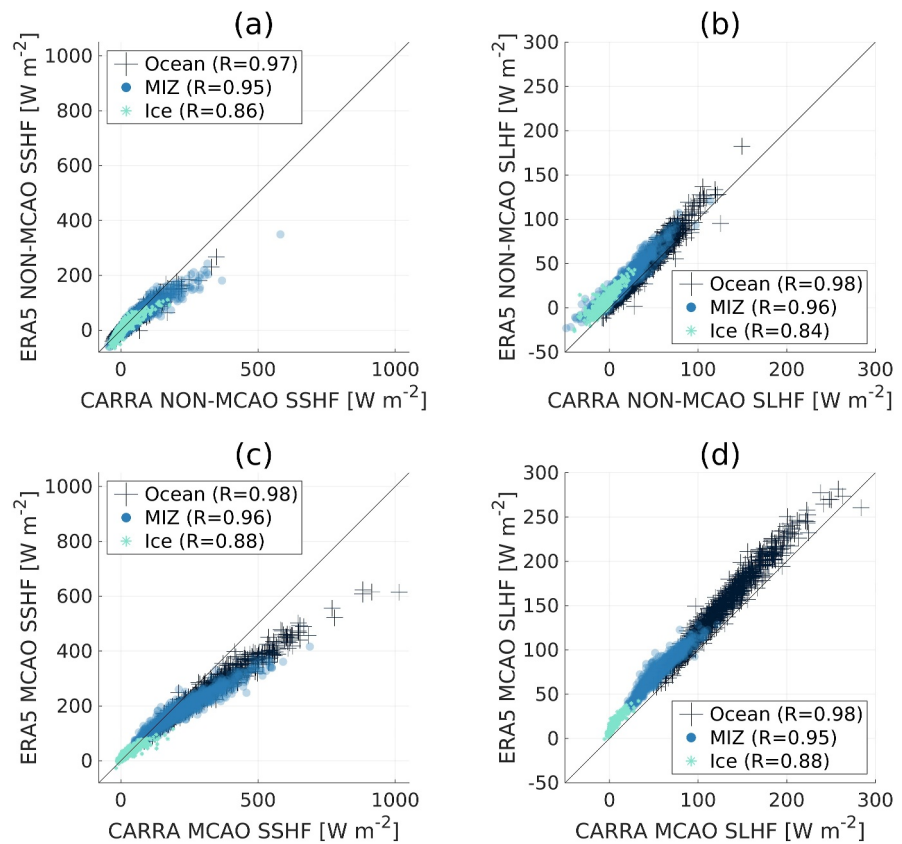


Figure 3. Daily mean CARRA versus ERA5 surface sensible heat flux (SSHF) and surface latent heat flux (SLHF) in the Fram Strait box (black box in Figure 1), November–March 1991–2020. Points over ice-free ocean (dark crosses), the marginal ice zone (MIZ; blue dots), and sea ice (bright stars) are shown for non-MCAO SSHF (CARRA MCAO index ≤ 0 K; a) and SLHF (b) as well as MCAO SSHF (CARRA MCAO index > 8 K; c) and SLHF (d). CARRA versus ERA5 correlation coefficients for each surface category are shown in the legends. To remove the effect of cyclicity, the correlations were computed on anomaly timeseries (i.e., from each daily mean value, the mean for that date in all the other years was subtracted). All correlations are statistically significant at the 95% confidence level.

(Figure 4d) during strong MCAOs. Although the SLHF clearly increases with the MCAO index for a given WS10, quite strong positive SLHF (up to 180 W m^{-2} in ERA5) are found also when the MCAO index is negative, reflecting that the surface-atmosphere humidity difference used to derive the SLHF may be positive even when the MCAO index is not.

Figure 4 also demonstrates that the degree to which the heat fluxes vary with the WS10 increases with the MCAO index, as the slope becomes steeper for higher MCAO index values. For example, for every ms^{-1} of WS10 variability, CARRA (ERA5) SSHF varies 9 W m^{-2} (7 W m^{-2}) when $0 \text{ K} < \text{MCAO index} \leq 2 \text{ K}$, while the corresponding number for $8 \text{ K} < \text{MCAO index} \leq 10 \text{ K}$ is 29 W m^{-2} (21 W m^{-2}), based on linear regression. Accurate representation of wind speed is thereby clearly important for the heat flux variability during MCAOs. We note that the WS10 tends to be somewhat higher in CARRA (Figure 4e), which has previously been found to match WS10 observations better than ERA5 (Køltzow et al., 2022), possibly due to the higher resolution (Kolstad, 2017).

4.2. Spatial Patterns

To better understand how the heat fluxes may change in response to changes in the $\theta_s - \theta_{850}$ difference forming the basis for our MCAO index, we examine the spatial patterns of the monthly mean trends (Figure 5). Since $\theta_s - \theta_{850}$ and the fluxes are heavily impacted by sea ice distribution (Taylor et al., 2018), we also include the SIC trends (Figures 5d, 5h, and 5l). WS10 trends were also computed, but are omitted since statistical significance was

Table 2
Marine Cold Air Outbreak Index and Wind Speed Versus Surface Heat Fluxes

Variables	R	R^2	b [$\text{Wm}^{-2}\text{K}^{-1}$]	$b\text{STD}_M$ (Wm^{-2})
MCAO versus SSHF	0.78 (0.83)	0.62 (0.7)	18 (15)	97 (78)
MCAO versus SLHF	0.79 (0.81)	0.62 (0.65)	6 (7)	33 (39)
Variables	R	R^2	b [$\text{Wm}^{-2}(\text{ms}^{-1})^{-1}$]	$b\text{STD}_W$ [Wm^{-2}]
WS10 versus SSHF	0.51 (0.47)	0.26 (0.22)	20 (14)	63 (44)
WS10 versus SLHF	0.59 (0.57)	0.35 (0.33)	8 (9)	24 (27)

Note. Coefficients from correlations (R) and regressions (b) of the daily Marine Cold Air Outbreak (MCAO) index and 10 m wind speed (WS10), respectively, with the surface sensible heat flux (SSHF) and the surface latent heat flux (SLHF). Shown are also the normalized regression coefficients (b multiplied with the standard deviation of each predictor; STD_M for MCAO and STD_W for WS10). Values for CARRA are followed by values for ERA5 in parentheses. All correlations and regressions are statistically significant at the 95% confidence level.

lacking. ERA5 and CARRA mainly show similar patterns so ERA5 is excluded from the following discussion, but its trends are displayed in Figure A2. Since the direction of some of the trends change between months, we consider trends in separate months in addition to the extended winter mean. Here, we include the trends for January and March, which show opposing trends in the $\theta_s - \theta_{850}$ difference as well as the heat fluxes. While March is the only month for which positive heat flux and $\theta_s - \theta_{850}$ trends are found in Fram Strait, the trend patterns in January resemble those found in November, December, and February, but are more pronounced.

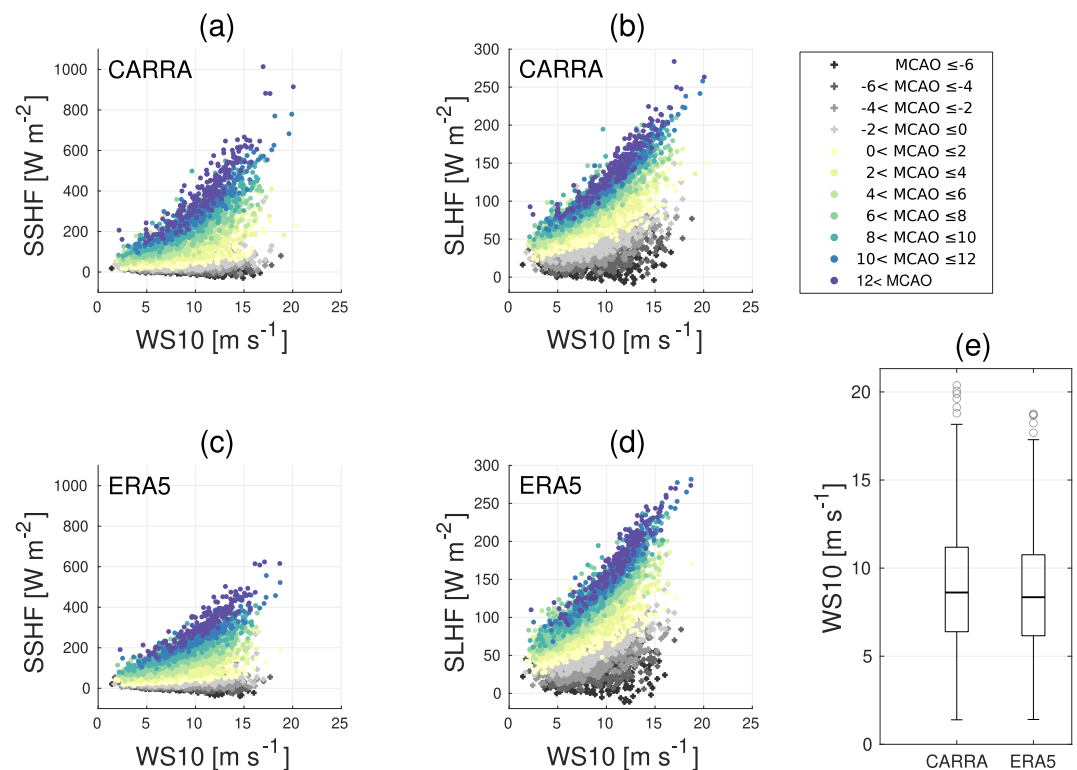


Figure 4. Daily mean 10 m wind speed (WS10) and surface heat fluxes for different Marine Cold Air Outbreak (MCAO) index classes (color-coded), for surface sensible heat flux (SSHF; a and c) and surface latent heat flux (SLHF; b and d) from CARRA (a and b) and ERA5 (c and d). WS10 in CARRA and ERA5 is shown in panel (e) as boxplots, where the black line in each box marks the median, the bottom (top) marks the 25th (75th) percentile and the whiskers extend to the most extreme value not considered an outlier, with outliers plotted as circles and defined as values >1.5 times the interquartile range outside the box. All data were averaged over the ice-free part of the Fram Strait box (black box in Figure 1).

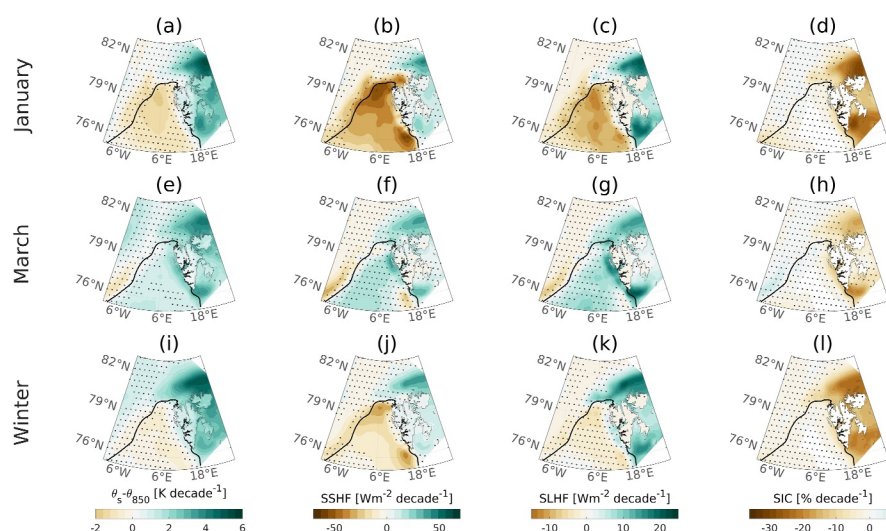


Figure 5. 1991–2020 CARRA trends in the surface-atmosphere potential temperature difference ($\theta_s - \theta_{850}$; a, e, and i), surface sensible heat flux (SSHF; b, f, and j), surface latent heat flux (SLHF; c, g, and k) and sea ice concentration (SIC; d, h, and l). Dotted denotes regions where the trend is not statistically significant at the 95% confidence level. The trends are based on monthly mean data for January (top row) and March (middle row), as well as extended winter mean data for November–March (bottom row). The black contour lines show the extended winter mean sea ice edge (SIC = 15%) from CARRA.

In January, significant negative $\theta_s - \theta_{850}$ trends (1–2 K per decade), SSHF trends (20–60 Wm⁻² per decade) and SLHF trends (5–15 Wm⁻² per decade) are found in ice-free Fram Strait (Figures 5a–5c). The negative $\theta_s - \theta_{850}$ trends are a result of the θ_{850} rising faster than the θ_s , as also seen in Dahlke et al. (2022). Meanwhile, pronounced positive trends are seen north, east and south of Svalbard, corresponding to areas of declining sea ice (Figure 5d). Negative winter heat flux trends in Fram Strait have previously been reported for the 1979–2008 period by Yu et al. (2013) and for the 2002–2020 period by Boisvert et al. (2022).

Positive trends in $\theta_s - \theta_{850}$ and heat fluxes are co-located with negative SIC trends around Svalbard in March as well (Figures 5e–5h). As noted above, the ice-free part of Fram Strait also exhibits positive trends in $\theta_s - \theta_{850}$ and the heat fluxes. However, statistical significance is lacking over large areas, particularly for SSHF. The $\theta_s - \theta_{850}$ trends and the resulting heat flux trends arise not only due to increasing θ_s , but also decreasing θ_{850} (not shown). This is consistent with the circulation change promoting northerlies in March (Dahlke et al., 2022), also seen as a negative temperature trend in the homogenized Ny-Ålesund radiosonde record (Maturilli & Kayser, 2017). Along the Svalbard west coast and in a small region in the southwestern part of the study area, the presence of negative SIC trends likely contributes to the heat flux trends.

In ice-free Fram Strait, the opposing monthly trends result in weak negative extended winter mean $\theta_s - \theta_{850}$ and heat flux trends (Figures 5i–5k). Significance is mostly lacking except for SSHF, which exhibits decreasing trends of around 10–40 Wm⁻² per decade. In ice-covered regions around Svalbard, the $\theta_s - \theta_{850}$ and heat fluxes have increasing trends, consistent with the decreasing SIC.

We investigate spatial patterns in the heat fluxes, WS10, 10 m wind direction, and $\theta_s - \theta_{850}$ as composites for the extended winter mean and MCAO anomalies (MCAO index > 8 K - mean) in Figure 6. For brevity, only CARRA is discussed here, but a corresponding figure for ERA5 is provided in the supplement (Figure A3).

As expected, the extended winter mean heat fluxes are greatest in ice-free Fram Strait, where the $\theta_s - \theta_{850}$ is large and the WS10 relatively high (Figures 6a–6d). Particularly high fluxes are found over the high SST of the WSC and along the northern ice edge. The SSHF shows its highest values in the latter region, where it approaches 250 Wm⁻². The SLHF distribution resembles the sea surface temperature (SST), with high values (110 Wm⁻²) along the WSC (Figure 6b).

During MCAOs, the anomalies in $\theta_s - \theta_{850}$ and the heat fluxes are shifted westwards (Figures 6e–6g). This is consistent with an anomalous westerly component in WS10 (Figure 6h), advecting cold air over the northwestern

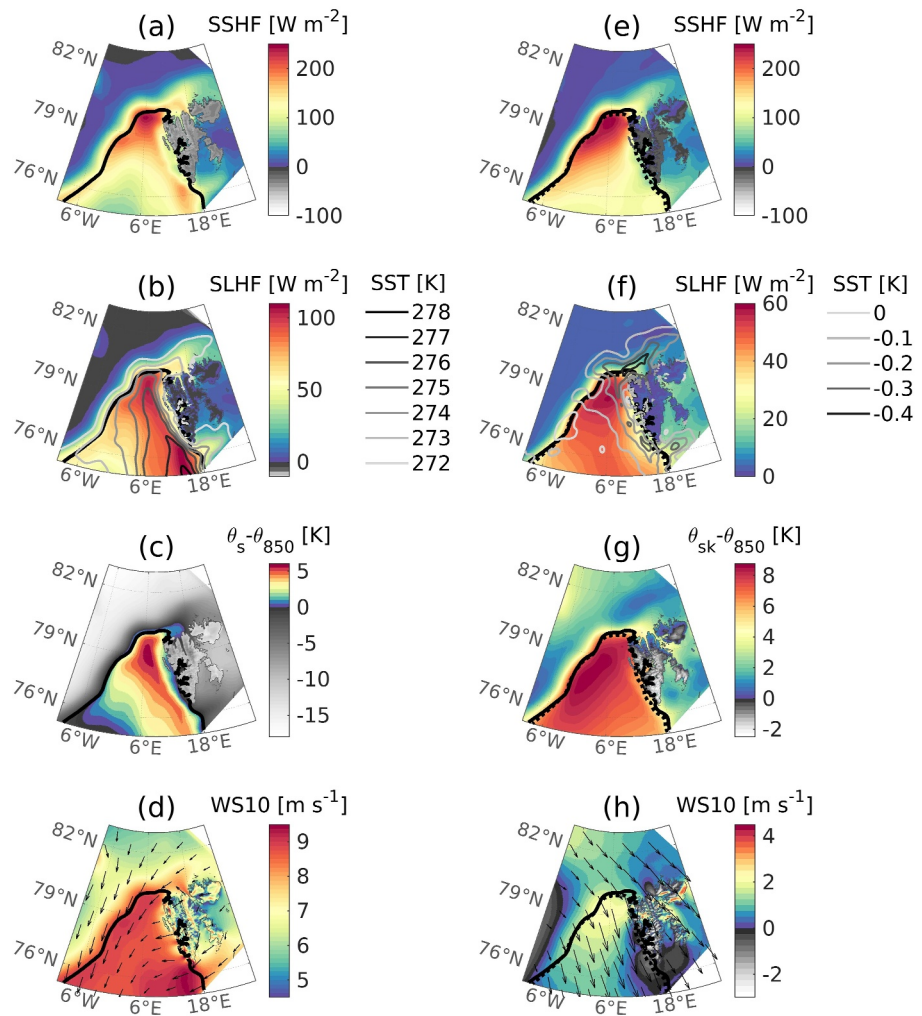


Figure 6. CARRA heat fluxes, surface-atmosphere potential temperature difference ($\theta_s - \theta_{sk-850}$), sea surface temperature (SST), and 10 m wind, for November–March 1991–2020. Mean conditions (left column) and Marine Cold Air Outbreak (MCAO) anomalies (right column) are shown for surface sensible heat flux (SSHf; a and e), surface latent heat flux (SLHF; b and f), SST (contour lines in b and f), $\theta_s - \theta_{sk-850}$ (c and g), and 10 m wind speed and direction (d and h). Black contours show the ice edge (CARRA SIC = 15%) for extended winter mean (solid lines) and MCAO conditions (dotted lines).

ice edge and thereby generating large temperature gradients promoting vigorous heat fluxes along the ice edge. In this region, the temperature at 850 hPa is 8 K lower than during mean conditions while the skin temperature hardly exhibits any anomalies (not shown), demonstrating that the large $\theta_s - \theta_{sk-850}$ difference during MCAOs results from changes in upper air temperature rather than surface temperature. This is in line with Kolstad et al. (2009), who found that atmospheric temperature variations are more important than SST variations for MCAO variability in the northern North Atlantic. The SSHf in this region is roughly doubled during MCAO conditions, when the flux is 250 W m^{-2} higher than in the extended winter mean. The SLHF shows a more moderate increase of 60 W m^{-2} .

To explore the vertical characteristics of MCAOs in the two reanalyses, we analyze CARRA and CARRA-ERA5 cross sections at 6°E and 79°N (Figures 7 and 8, respectively; pink dashed lines in Figure 1). CARRA is investigated from the surface to 300 hPa because this is the vertical span of the cold MCAO anomalies and includes most of the troposphere, which typically extends to around 270 hPa in the winter in this region (Zängl & Hoinka, 2001). In the CARRA-ERA5 difference plots, levels above 600 hPa are omitted to better demonstrate near-surface patterns (differences at higher levels are small and mainly concentrated at pressure levels that are absent in CARRA and therefore contains interpolated data). Non-negligible differences in wind speed and

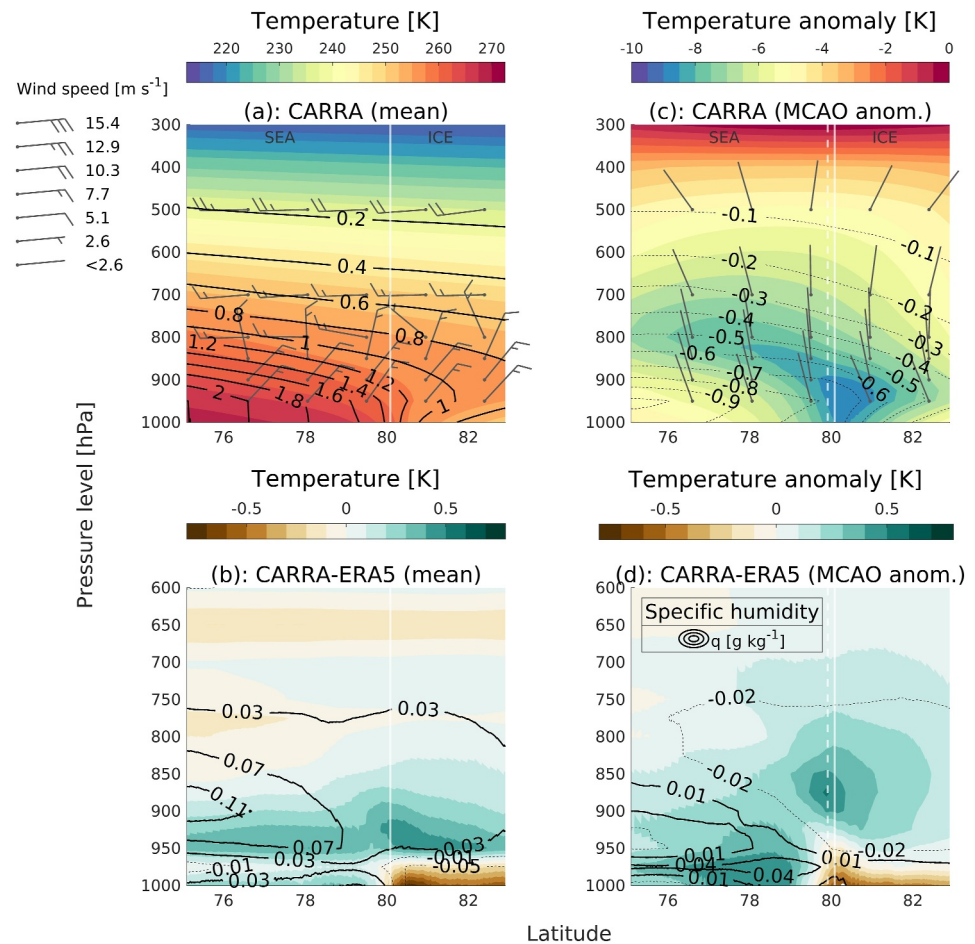


Figure 7. Cross sections at 6°E (pink dashed vertical line in Figure 1), from the surface to 300 hPa, showing temperature (colors), specific humidity (contour lines), and horizontal wind speed and direction (barbs), for November–March 1991–2020. Mean conditions are shown in the left column and Marine Cold Air Outbreak (MCAO) anomalies (MCAO index > 8 K - mean) are shown in the right column, for CARRA (a and c) and CARRA-ERA5 (b and d). Vertical lines denote transitions between regions dominated by sea ice or ocean (ICE and SEA, respectively), for mean conditions (solid) and MCAO conditions (dashed).

direction are confined to small regions that are not well represented by wind barbs, which are also omitted in the difference plots.

Near the surface, the extended winter mean temperature along the cross section at 6°E (Figure 7a) ranges from 273 K over the ocean in the south to 252 K above the sea ice in the north. The humidity distribution resembles the temperature distribution, with the highest values (2 g kg^{-1}) near the surface in the south. From 700 hPa and aloft, westerly winds prevail, while the lower atmosphere is dominated by northeasterly winds. The largest CARRA-ERA5 temperature difference is found in a shallow layer above the sea ice north of 80°N, where ERA5 is almost 0.8 K warmer (Figure 7b). It can be noted that ERA5 has a warm bias over sea ice (Wang et al., 2019) which has been related to the absence of snow on ice in ERA5 (Batra & Müller, 2019). The magnitude of the CARRA-ERA5 temperature difference is similar to Køltzow et al. (2022), who found an absolute difference between CARRA and ERA5 of 0.5–1 K over the sea ice north of Svalbard. Just above the surface layer, ERA5 is instead somewhat colder than CARRA, especially in the vicinity of the ice edge, where the difference reaches 0.5 K. The CARRA-ERA5 differences in specific humidity are largest around the 900 hPa level over the ocean in the south, where the specific humidity is 0.12 g kg^{-1} higher in CARRA. In the shallow layer above sea ice where ERA5 is warmer, the specific humidity is up to 0.07 g kg^{-1} higher in ERA5.

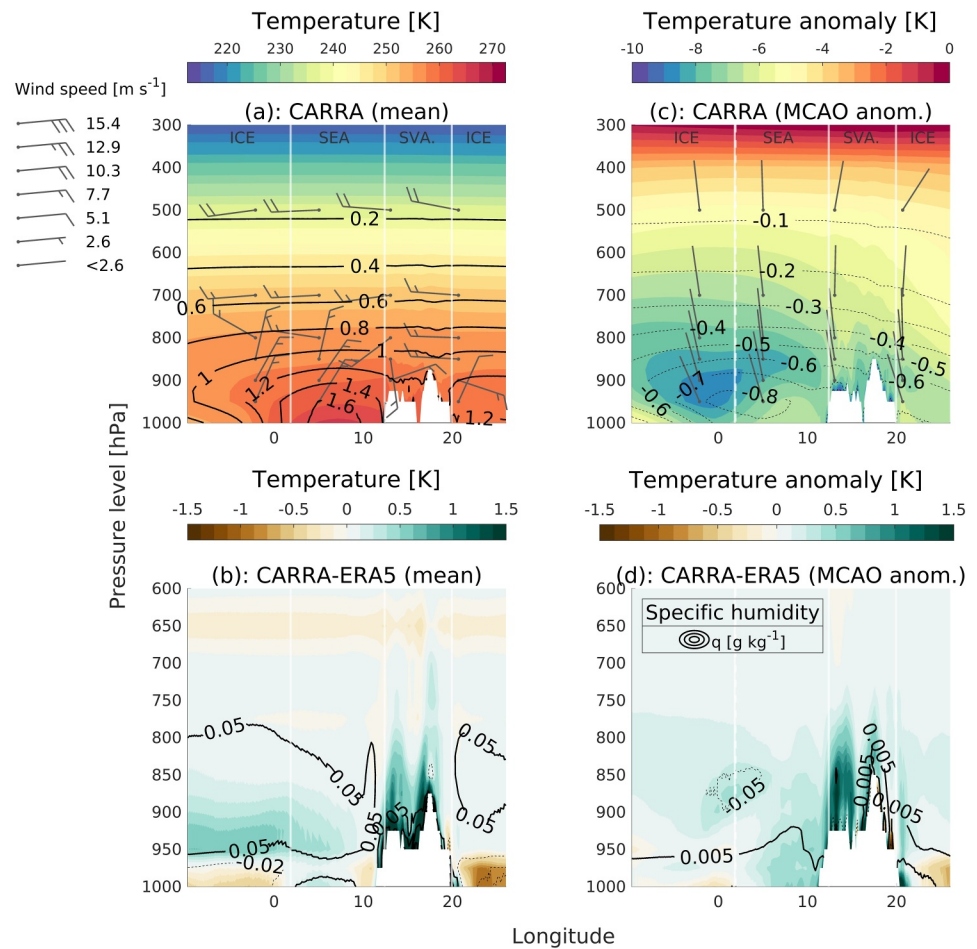


Figure 8. Cross sections at 79°N (pink dashed horizontal line in Figure 1), from the surface to 300 hPa, showing temperature (colors), specific humidity (contour lines), and horizontal wind speed and direction (barbs), for November–March 1991–2020. Mean conditions are shown in the left column and Marine Cold Air Outbreak (MCAO) anomalies (MCAO index > 8 K - mean) are shown in the right column, for CARRA (a and c) and CARRA-ERA5 (b and d). Vertical lines denote transitions between regions dominated by sea ice, ocean or land (ICE, SEA and SVA, respectively), for mean conditions (solid) and MCAO conditions (dashed).

During MCAO conditions, the wind shows anomalies with a northerly component throughout the troposphere (Figure 7c). The temperature and humidity are decreased everywhere, but the distributions of their anomalies differ. The specific humidity anomalies are strongest (exceeding -1 g kg^{-1}) over ice-free ocean in the south. At higher altitudes and over the sea ice, the anomalies are smaller since these regions are relatively dry in the mean conditions as well. The temperature anomalies are largest near the MIZ, reaching -9 K in CARRA. South of the ice edge the anomalies weaken with decreasing latitude, particularly near the surface, consistent with the progressive warming and boundary layer development seen in for example, Brümmer (1996); Kirbus et al. (2024). North of the ice edge, the anomalies decrease with increasing latitude, since the air over the ice is relatively cold also in the mean state. The cold MCAO anomalies are smaller in CARRA except for a shallow layer over the sea ice, where the cold anomalies are smaller in ERA5 (Figure 7d). The specific humidity difference is largest at the 975 hPa level, which is absent in CARRA, indicating that its exclusion may have impacted the representation of near-surface humidity in CARRA.

Along the cross section at 79°N (Figure 8a), the extended winter mean near-surface temperature in CARRA is highest (265.5 K) over the ice-free ocean and lowest (254.5 K) over the sea ice in the west. The specific humidity distribution follows the same pattern, and has its maximum (1.6 g kg^{-1}) over the ice-free ocean. The largest CARRA-ERA5 difference is seen over the land surface of Svalbard, where the temperature (specific humidity) is

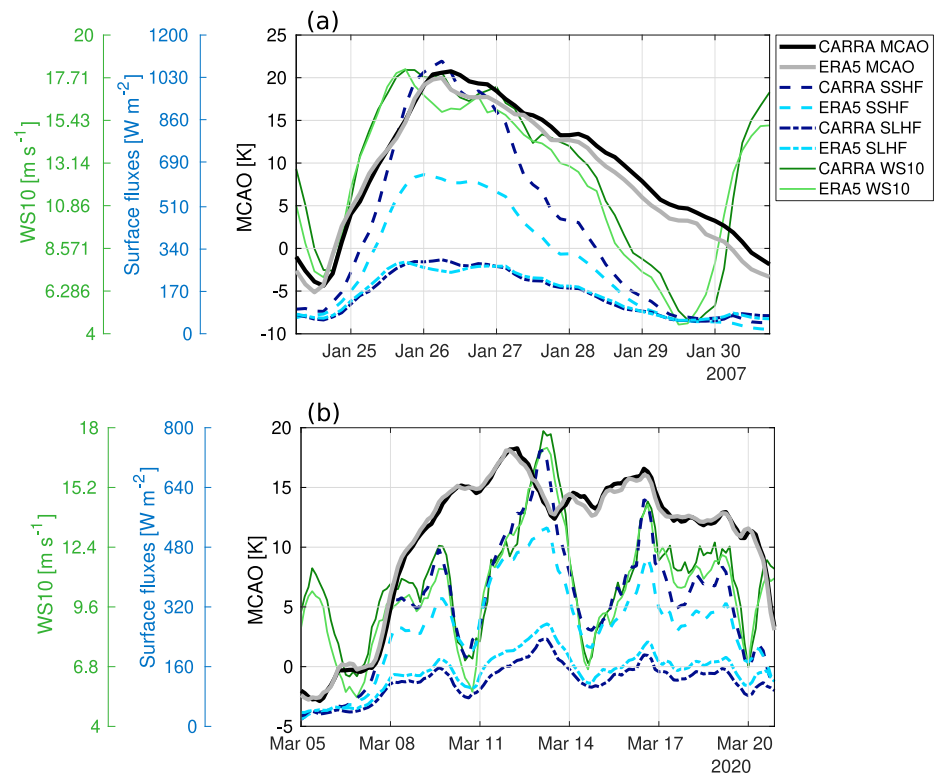


Figure 9. CARRA (darker shades) and ERA5 (lighter shades) 3-hourly Marine Cold Air Outbreak (MCAO) index, surface sensible heat flux (SSHF), surface latent heat flux (SLHF), and 10 m wind speed (WS10) during an MCAO in January 2007 (a) and an MCAO in March 2020 (b). The data were averaged over the ice-free fraction of the Fram Strait box (black box in Figure 1).

up to 4.5 K (0.4 g kg^{-1}) higher in CARRA (Figure 8b). For comparison, Køltzow et al. (2022) found that ERA5 underestimates the (2 m) temperature over Svalbard with biases of around -1.5 K in winter, while CARRA shows a much smaller overestimation. Similar to the cross section at 6°E , the specific humidity in the lowest levels is higher in CARRA (ERA5) over ocean (sea ice). It can be noted that in the MCAO case study by Kirbus et al. (2024), CARRA agreed better than ERA5 with observed specific humidity in the boundary layer over ice-free ocean, while the agreement in the two reanalyses was similar over sea ice.

The largest MCAO anomalies in humidity (around -1 g kg^{-1} in CARRA) are confined to one region over the Fram Strait, while large MCAO anomalies in temperature are found in two distinct regions (Figure 8c). One of these is situated near the ice edge close to 0°E , where anomalies of around -8 K are centered around the 900–950 hPa altitude. The second one is found over Svalbard below the 850 hPa level, where anomalies reach 7–10 K in CARRA, with the strongest anomalies confined to the lowermost levels. Similar to the CARRA-ERA5 temperature differences in the mean conditions, the CARRA-ERA5 differences in the MCAO anomalies are especially large over Svalbard (Figure 8d). In general, ERA5s cold anomalies are around 1 K larger in the region between the Svalbard land surface and the 800 hPa level. However, ERA5 shows smaller anomalies for some individual grid cells very close to the topography, indicating that the difference between the reanalyses is impacted by the lower horizontal resolution of ERA5. As for humidity, the near-surface (below 950 hPa) dry anomalies are larger in ERA5, especially over the sea ice east of Svalbard (Figure 8d). Above 950 hPa, the specific humidity anomalies are instead slightly higher (0.05 g kg^{-1}) in CARRA.

4.3. A Comparison of Two MCAO Cases

In the following, we use the three-hourly ice-free Fram Strait box MCAO indices, heat fluxes, and WS10 to investigate two individual MCAO cases. The first case takes place in January 2007 and features the highest MCAO index values of our entire study period (Figure 9a). The MCAO indices increase from negative values just

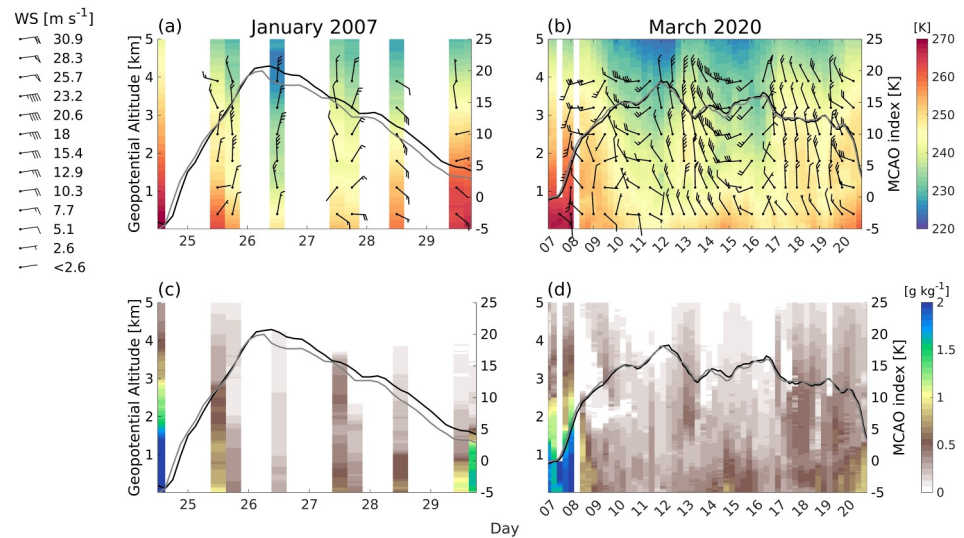


Figure 10. Ny-Ålesund radiosonde data for the Marine Cold Air Outbreak (MCAO) cases in January 2007 (a and c) and March 2020 (b and d). Air temperature and wind bars are shown in panels (a) and (b), specific humidity is shown in panels (c) and (d). The 3-hourly MCAO indices from CARRA (black) and ERA5 (gray) are shown on the right y-axis in each panel.

before the onset of the event (24 January 2007) to approximately 20 K during the peak, which occurs on 26 January 2007 at 09:00 (06:00) UTC in CARRA (ERA5). This rapid increase is followed by a roughly linear decline over the next few days, with the MCAO indices becoming negative on 30 January 2007. The WS10 is highest (18 ms^{-1}) on 25 January 2007 at 18:00 UTC and decreases over the next few days. This is in line with Kolstad (2017), who found that WS10 typically peaks 12 hr prior to the MCAO index in the Greenland-Iceland-Norwegian Seas and that the high wind speed only persists for a few days. The transient high wind speed may indicate the passage of baroclinic waves (Kolstad, 2017), in line with Fletcher et al. (2016) who found that strong MCAOs occur in the cold sector of extratropical cyclones. Consistent with the higher MCAO index and WS10, the CARRA-ERA5 SSHF difference is largest during the MCAO index peak, with CARRA exceeding $1,000 \text{ Wm}^{-2}$ and ERA5 reaching just over 600 Wm^{-2} . However, the SSHF is higher in CARRA before the peak too, with differences of up to 190 Wm^{-2} during the first half of 25 January 2007. These disparate SSHFs occur despite similar WS10 and MCAO index values, indicating that parameterization differences (Section 2) also play a role. The SLHF shows smaller temporal variability than the SSHF, with peak values barely reaching 300 Wm^{-2} . The largest SLHF difference (45 Wm^{-2}) is also found during the MCAO peak, when the SLHF is actually larger in CARRA. This is likely related to the temporal evolution of WS10 which shows a pronounced dip in ERA5 around the 26 January 2007, coinciding with the smaller ERA5 SLHF.

The second case took place in March 2020, that is, during a winter which featured an exceptionally strong stratospheric polar vortex along with a persistently positive Arctic Oscillation (AO) from January to March (Lawrence et al., 2020). The pressure anomalies accompanying the positive AO in Lawrence et al. (2020), specifically the low pressure anomaly in the eastern Arctic, is favorable for strong MCAOs (Dahlke et al., 2022). Notably, March 2020 did feature unusually high monthly mean MCAO index (Dahlke et al., 2022). This period also coincided with the COMBLE campaign (December 2019–May 2020; Geerts et al., 2022) in Andenes (Norway) and Bear Island, giving rise to MCAO studies focusing on the periods around 13 March (Lackner et al., 2023; Wu et al., 2025) and 28–29 March (Geerts et al., 2022; Zheng et al., 2024).

We focus on the period from 8 March (morning) to 20 March (noon), during which the CARRA and ERA5 MCAO indices remain above 8 K (Figure 9b). The highest MCAO index values (18 K) are found on 12 March, but in contrast to the first event, the second case is not characterized by one distinct peak. Instead, the MCAO index remains above 8 K over the entire period 8–20 March 2020. During this time the heat fluxes show stronger correlation with WS10 than the MCAO index in both reanalyses. Given the consistently high MCAO index and substantial variability in WS10, it is not surprising that the heat flux variability is largely governed by wind speed fluctuations during the event, in line with Figure 4. The CARRA-ERA5 SSHF difference is smaller than in the

January 2007 event, as expected given the smaller SSHF magnitude. The SLHF is consistently higher in ERA5, with a maximum difference of 50 Wm^{-2} . For both cases, WS10 is mostly higher in CARRA, in line with Kølitzow et al. (2022).

As seen in the cross sections in Figure 8, the temperature above Svalbard is heavily impacted by MCAOs. Therefore, we utilize radiosonde-data from Ny-Ålesund to provide a detailed observational record of the temporal evolution of the lower troposphere during the two MCAO cases (Figure 10). We focus on the lowermost 5 km of the atmosphere, where the strongest effects of MCAOs are found. Temperature and specific humidity data are plotted at 00:00 UTC, 06:00 UTC, 12:00 UTC, and 18:00 UTC, along with wind barbs showing the horizontal wind speed and direction. To avoid cluttering, the wind barbs are only shown for 00:00 UTC and 12 UTC in the March 2020 case. Ny-Ålesund is located at the southern coast of the Kongsfjord, surrounded by mountains and glaciers, so the lowermost part of the vertical column encounters local orographic effects. With their vertical resolution of ca 5 m (here interpolated to fixed 10 m steps), the radiosonde data can resolve fine structures that are not captured by the reanalyses.

The air temperature (Figure 10a) and specific humidity (Figure 10c) above Ny-Ålesund gradually decrease during the onset of the first event. The minimum values are recorded at 12 UTC on 26 January 2007, that is, by the first radiosonde launched after the MCAO index peak. At this time, the near surface air temperature (specific humidity) has fallen to 249 K (0.29 g kg^{-1}), which is 22 K colder (2.88 g kg^{-1} drier) than just before the onset of the event. Consistent with the temperature drop, the tropopause height falls from 9.1 km (256 hPa) on 25 January to 4.6 km (505 hPa) on 26 January (not shown), likely indicative of a front passage as noted above. Thereafter, the temperature and specific humidity increase with the decreasing MCAO index, as expected since the MCAO index largely reflects the atmospheric temperature evolution. The winds in the free troposphere are predominantly northerly between 25 and 27 January when the MCAO index is high, consistent with higher (lower) sea level pressure west (east) of Fram Strait resulting in the northerly geostrophic flow that is typical for MCAOs in this region (Dahlke et al., 2022; Kolstad, 2017).

As for the second case, a marked drop in near surface temperature and specific humidity is seen during the MCAO onset on 8 March 2020, but thereafter cold and dry conditions with comparatively small day-to-day variability prevail throughout the event (Figures 10b and 10d). The coldest and driest conditions are found on 12 March, with a near surface air temperature (specific humidity) of 243 K (0.19 g kg^{-1}). Meanwhile, the north-northwesterly flow seen in the radiosonde data as well as along the backward trajectory across Fram Strait in Wu et al. (2025) brings the cold air toward Andenes, where one of the stronger MCAO events of the COMBLE period was registered on 13 March (Lackner et al., 2023). The winds are predominantly northerly to westerly throughout the case, although easterly and southerly components are also present in a few instances. Northwesterly winds dominate in the lower kilometer. These northwesterly winds may be due to the geographical position of the fjord valley, which typically leads to wind channeling in a southeasterly, or, less commonly, northwesterly direction (Maturilli & Kayser, 2017). Overall, the comparison between the two events demonstrates that the temporal evolution and atmospheric conditions during MCAOs can vary substantially between individual cases. It also highlights the strong impact of MCAOs on Svalbard air temperature and specific humidity.

5. Discussion

In many parts of the Arctic, the heat fluxes are of growing importance for the climate system because of the strong trends in the surface-atmosphere temperature difference, mainly associated with sea ice decrease (Screen & Simmonds, 2010; Taylor et al., 2018). We also see increasing heat flux trends in regions with decreasing SIC, particularly around southeastern and northeastern Svalbard (Figure 5). At the same time, Arctic surface heat fluxes mostly take place in irregular bursts associated with episodic events like MCAOs (Papritz & Spengler, 2017; Taylor et al., 2018), implying that MCAO changes may also be important in determining the surface heat fluxes. As seen in Figure 2, the interannual variability of the heat fluxes in ice-free Fram Strait is strikingly similar to the MCAO index. However, in contrast to Dahlke et al. (2022) who found significant ERA5 MCAO index trends in December, January, and March, we only find significant MCAO index trends for CARRA in January (negative) and ERA5 in March (positive). The January trend in CARRA is also reflected in the significant negative heat flux trends for this month. For the extended winter mean, the opposing signs in March and mid-winter lead to weaker trends which are not significant except for

CARRA SSHF (not shown). The negative January MCAO index trend arises because the tropospheric warming trend is larger than the surface warming trend (Dahlke et al., 2022). Faster atmosphere than sea surface warming leading to increased tropospheric static stability and negative MCAO index trends over open ocean are projected to continue in the coming decades (Landgren et al., 2019). Future studies could further investigate how the changes in surface-atmosphere temperature difference is reflected in the frequency, duration, or intensity of MCAO events.

We have demonstrated large CARRA-ERA5 heat flux differences, highlighting the uncertainty in reanalysis-derived heat fluxes. The differences may result from the differing parameterization schemes as well as the meteorological variables used to compute the heat fluxes (temperature, humidity, and wind; Equations 1 and 2).

Regarding the higher SSHF in CARRA, the MCAO index is higher in CARRA (Figure 2), mainly due to higher skin temperature over ocean. The higher MCAO index is a very likely contributor to the higher SSHF, especially since the CARRA-ERA5 differences in the MCAO index and SSHF both decrease over the investigated period. The decreasing differences are likely related to the larger number of observations assimilated in the reanalysis production following increased availability of observations. In any case, the similar temporal evolution of the differences in the MCAO indices and the SSHF, respectively, indicates that the differences are affected by the temperature. The temperature in turn may be impacted by the differing representation of clouds in the two reanalyses. Due to its higher spatial resolution, CARRA permits convection, and (unlike ERA5) was capable of producing several distinct cloud streets during the MCAO studied by Kirbus et al. (2024). Outside summer, clouds warm the surface which affects the heat fluxes, especially over the sea ice (Taylor et al., 2018). For example, Persson et al. (2017) studied long-range advection into the Arctic Basin and found that the stratocumulus that formed warmed the surface and increased the SSHF. Stratocumulus are also common during the initial phases of MCAOs (Murray-Watson et al., 2023). It is probable that the better representation of clouds in CARRA affects the differences in surface temperature and thereby the SSHF. At the same time, SSHF is lower in ERA5 also over sea ice, despite ERA5 showing higher surface temperature and lower atmospheric temperature there (Figure 7), which in itself would promote higher SSHF in ERA5. The fact that SSHF still tends to be higher in CARRA is likely related to the higher WS10 in CARRA (Figure 4e). However, higher SSHF in CARRA can also be seen within a given WS10 and MCAO class (Figures 4a–4d). While direct comparisons are challenging due to variations in WS10 and the MCAO index within each designated class, this suggests that parameterization plays an additional role.

As for SLHF, this study does not examine the surface-atmosphere humidity difference, which could differ between the reanalyses. The humidity biases in ERA5 (Graham et al., 2019) and CARRA (Kirbus et al., 2024) vary with environmental conditions and at different altitudes. Again, parameterization may also play a role. For example, the roughness lengths for momentum (z_{0M}), heat (z_{0H}), and moisture (z_{0Q}) are not the same in the two reanalyses. We notice that while CARRA $z_{0M} = z_{0H} = z_{0Q}$ over ice-free ocean, ERA5 have larger z_{0Q} than z_{0H} , potentially contributing to the higher SLHF. A study focusing on the Pacific Arctic in July–December found that the parameterization scheme was not the dominant cause of differences between ERA5 and observation-derived heat fluxes calculated with a bulk algorithm (Kong et al., 2022). Instead, errors in air temperature and humidity played the larger role for the errors in SSHF and SLHF, respectively. However, the relative contributions from meteorological variables and parameterization may vary with local conditions. Future studies could perform model experiments dedicated to disentangling the effects of differences in meteorological parameters and parameterization, respectively.

Because no heat flux measurements from the Fram Strait were available for our study period, we cannot conclude whether CARRA or ERA5 agrees best with observation-derived heat fluxes. However, CARRA was produced specifically for the Arctic environment and is generally expected to benefit from improvements with respect to ERA5, for example, regarding the treatment of cold surfaces and the higher horizontal resolution (Yang et al., 2020). Early evaluations have also presented arguments in favor of CARRA, such as better agreement with observations of surface temperature and WS10 (Køltzow et al., 2022). Recently, a first evaluation of CARRA and ERA5 during a Fram Strait MCAO found that CARRA SSHF agreed better with observation-derived SSHF and suggested that the too wide MIZ in ERA5 leads to heat flux underestimations during the first 2–3 hr of the MCAO (Kirbus et al., 2024). Biases in temperature, wind speed, and heat fluxes over the MIZ in ERA5 have also been related to ERA5s poor representation of the MIZ in previous studies (Renfrew et al., 2021). The better agreement of CARRA with observation-derived SSHF in Kirbus et al. (2024), along with the fact that we consistently see the

same pattern of CARRA-ERA5 SSHF difference in our study (Figure 3) hints towards the tentative conclusion that SSHF is better represented by CARRA, also in absence of MCAO conditions. For SLHF, however, the picture is less clear. Compared with heat fluxes derived with a bulk algorithm using meteorological data from the Iceland Sea in late winter and spring, ERA5 has been found to overestimate the SLHF (Renfrew et al., 2021). Moreover, Kirbus et al. (2024) found that ERA5 tends to produce too much liquid-bearing clouds and precipitation, leading to a too dry marine boundary layer during their MCAO case. At the same time, Kirbus et al. (2024) only found overestimated ERA5 SLHF during the first hour of the event. Thereafter, both CARRA and ERA5 underestimated the SLHF, with ERA5 being slightly closer to the observation-derived SLHF. It is thereby clear that more studies comparing the reanalyses to observation-derived heat fluxes during different meteorological conditions, including MCAOs, are needed. Special attention should be given to the role of clouds, given their differing representation in the two reanalyses and their influence on the heat fluxes.

MCAOs are commonly defined as advection of polar or cold continental air over open ocean, and typically result in instability promoting large heat fluxes and severe weather (e.g., Brümmner, 1997; Fletcher et al., 2016; Papritz et al., 2019; Terpstra et al., 2021). However, the March 2020 case exemplifies that meteorological conditions may vary substantially during an MCAO, raising the question of what truly constitutes “MCAO conditions.” It could be argued that MCAO conditions do not prevail during the periods around 10 March and 14 March when pronounced dips are seen in WS10 and the heat fluxes (Figure 9b), along with warmer and more humid conditions in Ny-Ålesund (especially for the latter period; Figures 10b and 10d). Some studies have taken further criteria into account when defining MCAOs. For example, Lackner et al. (2023) required onshore wind (in Andenes, Norway) and wind speed above 5 m/s in addition to a positive MCAO index. The choice of MCAO index threshold could also be adjusted. Such approaches may exclude briefer periods during which wind speed and heat fluxes decrease despite a large surface-atmosphere temperature gradient, and ensure that only typical MCAO conditions with high heat fluxes are included.

6. Summary and Conclusions

We investigated Marine Cold Air Outbreak (MCAO) conditions and surface turbulent heat fluxes in Svalbard and Fram Strait using reanalysis data from ERA5 and CARRA, spanning November–March 1991–2020. For each reanalysis, we calculated an MCAO index based on the potential temperature difference between the surface and 850 hPa ($\theta_s - \theta_{850}$). In addition to statistical analysis of the atmospheric characteristics associated with MCAOs and their effects on the heat fluxes, we investigated two separate cases using the reanalysis data and radiosonde data from Ny-Ålesund, Svalbard.

We found that the surface sensible heat flux (SSHF) in Fram Strait is substantially higher in CARRA than in ERA5, for the extended winter mean as well as strong MCAO conditions (MCAO index > 8 K). The surface latent heat flux (SLHF), in contrast, is consistently somewhat lower. For SSHF, the largest differences exceed 300 W m^{-2} and are found over ice-free ocean, where the SSHF itself is large. Normalizing these differences relative to heat flux strength over each surface (sea ice, marginal ice zone, and ocean) reveals notable discrepancies over sea ice-covered areas. Here, particularly large differences are seen for SLHF during strong MCAO conditions, when ERA5 SLHF represents 263% of the interquartile range (IQR) of CARRA SLHF over sea ice.

The spatial patterns in the positive heat flux trends mirror the sea ice decline around much of Svalbard. In ice-free Fram Strait, however, the strength, direction, and significance of the trends are inconsistent. The most pronounced trends are found in January, when the heat fluxes are declining in response to a stronger temperature increase at 850 hPa than at the surface.

During MCAO conditions, the heat fluxes from the ocean to the atmosphere are greatly enhanced, particularly in the northern and northwestern part of the ice-free Fram Strait. In this area, the SSHF is roughly doubled during strong MCAOs. In the vertical, negative MCAO anomalies in air temperature and specific humidity are present throughout most of the troposphere. The specific humidity anomalies tend to be largest over the ice-free ocean in southern Fram Strait while the largest temperature anomalies are found near the ice edge and in the surface layers over Svalbard. The large impact of Fram Strait MCAOs on Svalbard is also demonstrated in the radiosonde record of two individual MCAO events. Our study thereby sheds light on the atmospheric conditions and ocean-atmosphere heat fluxes during MCAOs in the gateway to the Arctic, where the exchanges and distribution of heat are of great importance for the enhanced Arctic warming.

Appendix A: Supplementary Figures

We used an Marine Cold Air Outbreak (MCAO) index threshold of 8 K to calculate composites of strong MCAOs. Adjusting the threshold would affect the magnitude of the MCAO anomalies, as exemplified in Figure A1, showing CARRA MCAO anomalies in air temperature and specific humidity based on the thresholds 4 K (Figure A1a), 8 K (Figure A1b), and 12 K (Figure A1c). In Section 4.2, we show CARRA trends and MCAO composites. For completeness, we show the ERA5 trends (Figure A2) and MCAO composites (Figure A3) below.

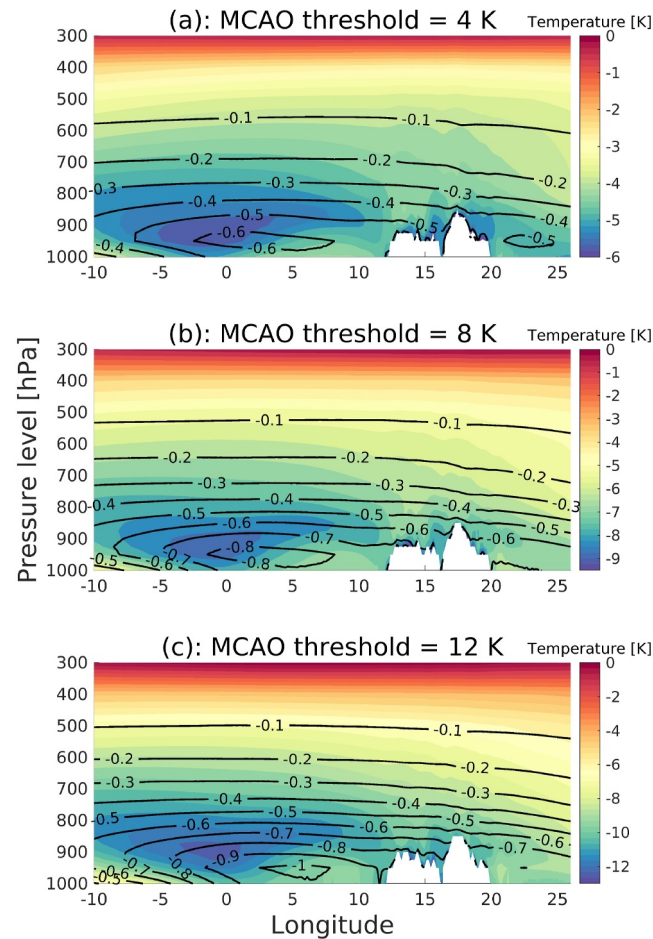


Figure A1. CARRA Marine Cold Air Outbreak (MCAO) anomalies for the cross section at 79°N (pink dashed horizontal line in Figure 1), from the surface to 300 hPa, showing temperature (colors) and specific humidity (contour lines), for November–March 1991–2020. The anomalies are calculated as MCAO conditions minus winter mean conditions, with MCAOs defined by three different thresholds for the surface-atmosphere temperature difference; 4 K (a), 8 K (b), and 12 K (c).

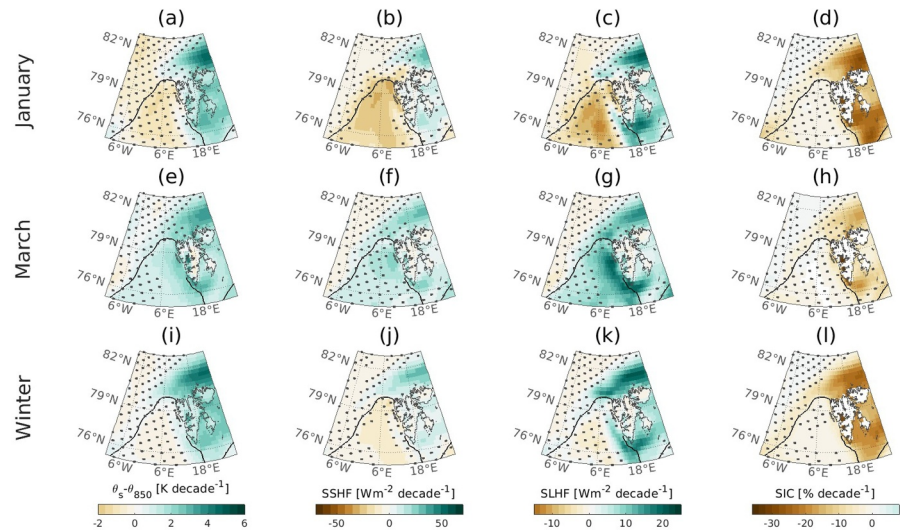


Figure A2. 1991–2020 ERA5 trends in the surface-atmosphere potential temperature difference ($\theta_s - \theta_{850}$; a, e, and i), surface sensible heat flux (SSHF; b, f, and j), surface latent heat flux (SLHF; c, g, and k), and sea ice concentration (SIC; d, h, and l). Dotted regions denote areas where the trend is not statistically significant at the 95% confidence level. The trends are based on monthly mean data for January (top row) and March (middle row), as well as extended winter mean data for November–March (bottom row). The black contour lines show the extended winter mean sea ice edge (SIC = 15%) from ERA5.

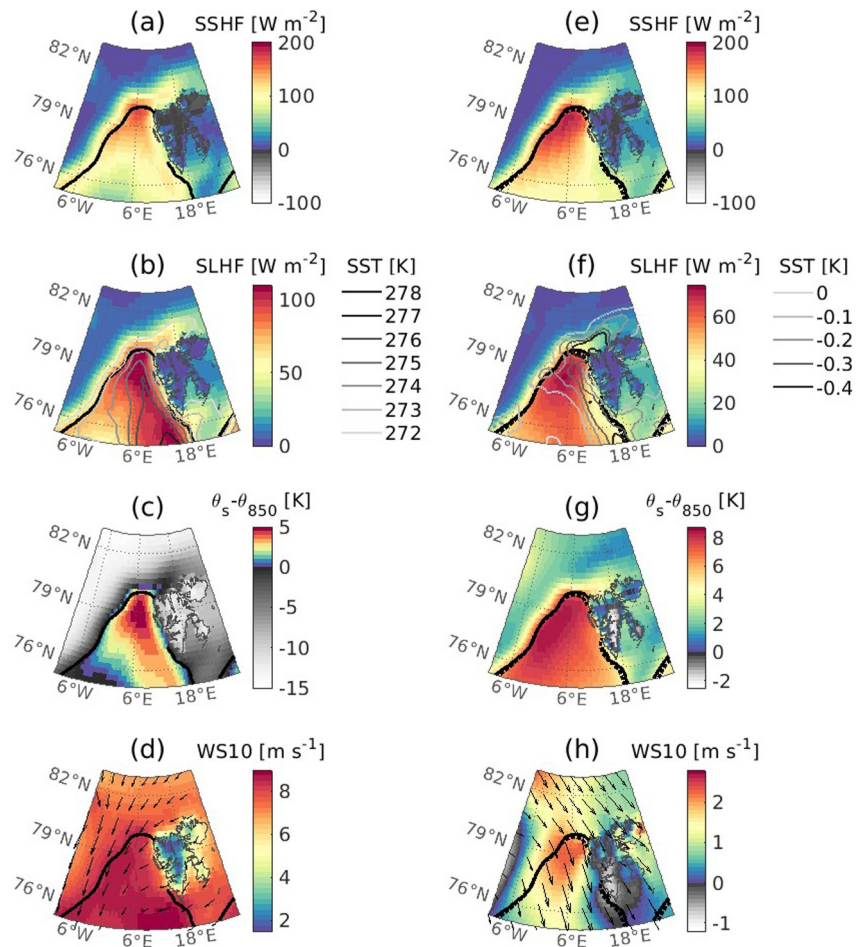


Figure A3. ERA5 heat fluxes, surface-atmosphere potential temperature difference ($\theta_s - \theta_{850}$), sea surface temperature (SST), and 10 m wind, for November–March 1991–2020. Mean conditions (left column) and Marine Cold Air Outbreak (MCAO) anomalies (right column) are shown for surface sensible heat flux (SSHF; a and e), surface latent heat flux (SLHF; b and f), SST (contour lines in b and f), $\theta_s - \theta_{850}$ (c and g) and 10 m wind speed and direction (d and h). Black contours show the ice edge (ERA5 SIC = 15%) for extended winter mean (solid lines) and MCAO conditions (dotted lines).

Data Availability Statement

All data used in this study are publicly available. The CARRA (Schyberg et al., 2020a, 2020b) reanalysis data were downloaded from the Copernicus Climate Change Service (C3S) Climate Data Store (CDS; registration required): <https://cds.climate.copernicus.eu/datasets/reanalysis-carra-pressure-levels?tab=overview> and <https://cds.climate.copernicus.eu/datasets/reanalysis-carra-single-levels?tab=overview>. The ERA5 reanalysis data (Hersbach et al., 2017, 2018) are available from the MARS tape archive (<https://apps.ecmwf.int/data-catalogues/era5/?class=ea>) and CDS (registration required): <https://cds.climate.copernicus.eu/datasets/reanalysis-era5-single-levels?tab=overview> and <https://cds.climate.copernicus.eu/datasets/reanalysis-era5-pressure-levels?tab=overview>. The results contain modified Copernicus Climate Change Service information 2022. Neither the European Commission nor ECMWF is responsible for any use that may be made of the Copernicus information or data it contains. The Ny-Ålesund radiosonde data (Maturilli, 2008, 2020) are available from the PANGAEA database without registration: <https://doi.org/10.1594/PANGAEA.695515> and <https://doi.org/10.1594/PANGAEA.917966>.

Acknowledgments

We gratefully acknowledge the funding by the Deutsche Forschungsgemeinschaft (DFG, German Research Foundation)—project no. 268020496—TRR 172, within the Transregional Collaborative Research Center “Arctic Amplification: Climate Relevant Atmospheric and Surface Processes, and Feedback Mechanisms (AC³.” We would also like to thank the staff of the AWIPEV research base in Ny-Ålesund for the radiosonde launches contributing to this study.

References

Aagaard, K., & Greisman, P. (1975). Toward new mass and heat budgets for the Arctic Ocean. *Journal of Geophysical Research*, *80*(27), 3821–3827. <https://doi.org/10.1029/jc080i027p03821>

Aue, L., Vihma, T., Uotila, P., & Rinke, A. (2022). New insights into cyclone impacts on sea ice in the Atlantic sector of the Arctic Ocean in winter. *Geophysical Research Letters*, *49*(22), e2022GL100051. <https://doi.org/10.1029/2022gl100051>

Batrak, Y., & Müller, M. (2019). On the warm bias in atmospheric reanalyses induced by the missing snow over Arctic sea-ice. *Nature Communications*, *10*(1), 1–8.

Beljaars, A. C. (1995). The parametrization of surface fluxes in large-scale models under free convection. *Quarterly Journal of the Royal Meteorological Society*, *121*(522), 255–270. <https://doi.org/10.1002/qj.49712152203>

Bengtsson, L., Andrae, U., Aspelién, T., Batrak, Y., Calvo, J., de Rooy, W., et al. (2017). The HARMONIE–AROME model configuration in the ALADIN–HIRLAM NWP system. *Monthly Weather Review*, *145*(5), 1919–1935. <https://doi.org/10.1175/mwr-d-16-0417.1>

Boisvert, L., Boeke, R., Taylor, P., & Parker, C. (2022). Constraining Arctic climate projections of wintertime warming with surface turbulent flux observations and representation of surface–atmosphere coupling. *Frontiers in Earth Science*, *10*, 765304. <https://doi.org/10.3389/feart.2022.765304>

Brümmer, B. (1996). Boundary-layer modification in wintertime cold-air outbreaks from the Arctic sea ice. *Boundary-Layer Meteorology*, *80*(1–2), 109–125. <https://doi.org/10.1007/bf00119014>

Brümmer, B. (1997). Boundary layer mass, water, and heat budgets in wintertime cold-air outbreaks from the Arctic sea ice. *Monthly Weather Review*, *125*(8), 1824–1837. [https://doi.org/10.1175/1520-0493\(1997\)125<1824:blmwah>2.0.co;2](https://doi.org/10.1175/1520-0493(1997)125<1824:blmwah>2.0.co;2)

Brümmer, B., Müller, G., Affeld, B., Gerdes, R., Karcher, M., & Kauker, F. (2001). Cyclones over fram strait: Impact on sea ice and variability. *Polar Research*, *20*(2), 147–152. <https://doi.org/10.3402/polar.v20i2.6511>

Brümmer, B., & Pohlmann, S. (2000). Wintertime roll and cell convection over Greenland and Barents Sea regions: A climatology. *Journal of Geophysical Research*, *105*(D12), 15559–15566. <https://doi.org/10.1029/1999jd900841>

Brutsaert, W. (1982). *Evaporation into the atmosphere: Theory, history and applications*. Reidel.

Charnock, H. (1955). Wind stress on a water surface. *Quarterly Journal of the Royal Meteorological Society*, *81*(350), 639–640. <https://doi.org/10.1002/qj.49708135027>

Dahlke, S., & Maturilli, M. (2017). Contribution of atmospheric advection to the amplified winter warming in the Arctic North Atlantic region. *Advances in Meteorology*, *2017*, 1–8. <https://doi.org/10.1155/2017/4928620>

Dahlke, S., Solbès, A., & Maturilli, M. (2022). Cold air outbreaks in fram strait: Climatology, trends, and observations during an extreme season in 2020. *Journal of Geophysical Research: Atmospheres*, *127*(3), e2021JD035741. <https://doi.org/10.1029/2021jd035741>

ECMWF. (2016). IFS documentation – Cy41r2. In *Operational implementation 8 March 2016 PART IV: Physical processes*. Retrieved from <https://www.ecmwf.int/sites/default/files/elibrary/2016/16648-part-iv-physical-processes.pdf#section.3.6>

Fearon, M. G., Doyle, J. D., Ryglicki, D. R., Finocchio, P. M., & Sprenger, M. (2021). The role of cyclones in moisture transport into the Arctic. *Geophysical Research Letters*, *48*(4), e2020GL090353. <https://doi.org/10.1029/2020gl090353>

Fletcher, J., Mason, S., & Jakob, C. (2016). The climatology, meteorology, and boundary layer structure of marine cold air outbreaks in both hemispheres. *Journal of Climate*, *29*(6), 1999–2014. <https://doi.org/10.1175/jcli-d-15-0268.1>

Geerts, B., Giangrande, S. E., McFarquhar, G. M., Xue, L., Abel, S. J., Comstock, J. M., et al. (2022). The COMBLE campaign: A study of marine boundary layer clouds in arctic cold-air outbreaks. *Bulletin of the American Meteorological Society*, *103*(5), E1371–E1389. <https://doi.org/10.1175/bams-d-21-0044.1>

Graham, R. M., Hudson, S. R., & Maturilli, M. (2019). Improved performance of ERA5 in Arctic gateway relative to four global atmospheric reanalyses. *Geophysical Research Letters*, *46*(11), 6138–6147. <https://doi.org/10.1029/2019gl082781>

Hartmann, J., Kottmeier, C., & Raasch, S. (1997). Roll vortices and boundary-layer development during a cold air outbreak. *Boundary-Layer Meteorology*, *84*(1), 45–65. <https://doi.org/10.1023/a:1000392931768>

Hersbach, H., Bell, B., Berrisford, P., Biavati, G., Horányi, A., Muñoz Sabater, J., et al. (2018). ERA5 hourly data on single levels from 1959 to present [Dataset]. *Copernicus Climate Change Service (C3S) Climate Data Store (CDS)*. <https://doi.org/10.24381/cds.adbb2d47>

Hersbach, H., Bell, B., Berrisford, P., Hirahara, S., Horányi, A., Muñoz-Sabater, J., et al. (2020). The ERA5 global reanalysis. *Quarterly Journal of the Royal Meteorological Society*, *146*(730), 1999–2049. <https://doi.org/10.1002/qj.3803>

Hersbach, H., Bell, B., Berrisford, P., Hirahara, S., Horányi, A., Muñoz-Sabater, J., et al. (2017). Complete ERA5 from 1979: Fifth generation of ECMWF atmospheric reanalyses of the global climate [Dataset]. *Copernicus Climate Change Service (C3S) Data Store (CDS)*. <https://doi.org/10.24381/cds.bd0915c6>

Kirbus, B., Schirmacher, I., Klingebiel, M., Schäfer, M., Ehrlich, A., Slättberg, N., et al. (2024). Thermodynamic and cloud evolution in a cold-air outbreak during HALO-(AC) 3: Quasi-Lagrangian observations compared to the ERA5 and CARRA reanalyses. *Atmospheric Chemistry and Physics*, *24*(6), 3883–3904. <https://doi.org/10.5194/acp-24-3883-2024>

Knudsen, E. M., Heinold, B., Dahlke, S., Bozem, H., Crewell, S., Gorodetskaya, I. V., et al. (2018). Meteorological conditions during the ALOUD/PASCAL field campaign near Svalbard in early summer 2017. *Atmospheric Chemistry and Physics*, *18*(24), 17995–18022. <https://doi.org/10.5194/acp-18-17995-2018>

Kolstad, E. W. (2011). A global climatology of favourable conditions for polar lows. *Quarterly Journal of the Royal Meteorological Society*, *137*(660), 1749–1761. <https://doi.org/10.1002/qj.888>

Kolstad, E. W. (2017). Higher ocean wind speeds during marine cold air outbreaks. *Quarterly Journal of the Royal Meteorological Society*, *143*(706), 2084–2092. <https://doi.org/10.1002/qj.3068>

Kolstad, E. W., & Bracegirdle, T. J. (2008). Marine cold-air outbreaks in the future: An assessment of IPCC AR4 model results for the northern hemisphere. *Climate Dynamics*, *30*(7–8), 871–885. <https://doi.org/10.1007/s00382-007-0331-0>

Kolstad, E. W., Bracegirdle, T. J., & Seierstad, I. A. (2009). Marine cold-air outbreaks in the North Atlantic: Temporal distribution and associations with large-scale atmospheric circulation. *Climate Dynamics*, *33*(2–3), 187–197. <https://doi.org/10.1007/s00382-008-0431-5>

Költzow, M., Schyberg, H., Støylen, E., & Yang, X. (2022). Value of the Copernicus Arctic Regional Reanalysis (CARRA) in representing near-surface temperature and wind speed in the north-east European Arctic. *Polar Research*, *41*. <https://doi.org/10.33265/polar.v41.8002>

Kong, B., Liu, N., Fan, L., Lin, L., Yang, L., Chen, H., et al. (2022). Evaluation of surface meteorology parameters and heat fluxes from CFSR and ERA5 over the pacific arctic region. *Quarterly Journal of the Royal Meteorological Society*, *148*(747), 2973–2990. <https://doi.org/10.1002/qj.4346>

Lackner, C. P., Geerts, B., Juliano, T. W., Xue, L., & Kosovic, B. (2023). Vertical structure of clouds and precipitation during arctic cold-air outbreaks and warm-air intrusions: Observations from COMBLE. *Journal of Geophysical Research: Atmospheres*, *128*(13), e2022JD038403. <https://doi.org/10.1029/2022jd038403>

- Landgren, O. A., Seierstad, I. A., & Iversen, T. (2019). Projected future changes in marine cold-air outbreaks associated with polar lows in the northern north-atlantic ocean. *Climate Dynamics*, 53(5–6), 2573–2585. <https://doi.org/10.1007/s00382-019-04642-2>
- Lawrence, Z. D., Perlwitz, J., Butler, A. H., Manney, G. L., Newman, P. A., Lee, S. H., & Nash, E. R. (2020). The remarkably strong arctic stratospheric polar vortex of winter 2020: Links to record-breaking arctic oscillation and ozone loss. *Journal of Geophysical Research: Atmospheres*, 125(22), e2020JD033271. <https://doi.org/10.1029/2020jd033271>
- Le Moigne. (2013). Surfex scientific documentation. Retrieved from <http://www.umar-cnrm.fr/surfex/spip.php?rubrique11>
- López-Moreno, J., Boike, J., Sanchez-Lorenzo, A., & Pomeroy, J. (2016). Impact of climate warming on snow processes in Ny-Ålesund, a polar maritime site at Svalbard. *Global and Planetary Change*, 146, 10–21. <https://doi.org/10.1016/j.gloplacha.2016.09.006>
- Louis, J.-F. (1979). A parametric model of vertical eddy fluxes in the atmosphere. *Boundary-Layer Meteorology*, 17(2), 187–202. <https://doi.org/10.1007/bf00117978>
- Masson, V., Le Moigne, P., Martin, E., Faroux, S., Alias, A., Alkama, R., et al. (2013). The surfexv7. 2 land and ocean surface platform for coupled or offline simulation of earth surface variables and fluxes. *Geoscientific Model Development*, 6(4), 929–960. <https://doi.org/10.5194/gmd-6-929-2013>
- Maturilli, M. (2008). Radiosonde measurements from station Ny-Ålesund (2007-01) [Dataset]. *Alfred Wegener Institute - Research Unit Potsdam, PANGAEA*. <https://doi.org/10.1594/PANGAEA.695515>
- Maturilli, M. (2020). High resolution radiosonde measurements from station Ny-Ålesund (2020-03) [Dataset]. *Alfred Wegener Institute - Research Unit Potsdam, PANGAEA*. <https://doi.org/10.1594/PANGAEA.917966>
- Maturilli, M., & Kayser, M. (2017). Arctic warming, moisture increase and circulation changes observed in the Ny-Ålesund homogenized radiosonde record. *Theoretical and Applied Climatology*, 130(1–2), 1–17. <https://doi.org/10.1007/s00704-016-1864-0>
- Meyer, M., Polkova, I., Modali, K. R., Schaffer, L., Baehr, J., Olbrich, S., & Rautenhaus, M. (2021). Interactive 3-D visual analysis of ERA5 data: Improving diagnostic indices for marine cold air outbreaks and polar lows. *Weather and Climate Dynamics*, 2(3), 867–891. <https://doi.org/10.5194/wcd-2-867-2021>
- Michaelis, J., Schmitt, A. U., Lüpkes, C., Hartmann, J., Birnbaum, G., & Vihma, T. (2022). Observations of marine cold-air outbreaks: A comprehensive data set of airborne and dropsonde measurements from the Springtime Atmospheric Boundary Layer Experiment (STABLE). *Earth System Science Data*, 14(4), 1621–1637. <https://doi.org/10.5194/essd-14-1621-2022>
- Murray-Watson, R. J., Gryspeerdt, E., & Goren, T. (2023). Investigating the development of clouds within marine cold-air outbreaks. *Atmospheric Chemistry and Physics*, 23(16), 9365–9383. <https://doi.org/10.5194/acp-23-9365-2023>
- Nielsen, Y., Agersten, D., & Køltzow, Ø. (2022). Copernicus Arctic regional reanalysis (CARRA): Data user guide. Retrieved from <https://confluence.ecmwf.int/display/CKB/Copernicus+Arctic+Regional+Reanalysis+%28CARRA%29%3A+Data+User+Guide>
- Papritz, L., Pfahl, S., Sodemann, H., & Wernli, H. (2015). A climatology of cold air outbreaks and their impact on air–sea heat fluxes in the high-latitude south pacific. *Journal of Climate*, 28(1), 342–364. <https://doi.org/10.1175/jcli-d-14-00482.1>
- Papritz, L., Rouges, E., Aemisegger, F., & Wernli, H. (2019). On the thermodynamic preconditioning of arctic air masses and the role of tropopause polar vortices for cold air outbreaks from fram strait. *Journal of Geophysical Research: Atmospheres*, 124(21), 11033–11050. <https://doi.org/10.1029/2019jd030570>
- Papritz, L., & Spengler, T. (2017). A Lagrangian climatology of wintertime cold air outbreaks in the Irminger and Nordic Seas and their role in shaping air–sea heat fluxes. *Journal of Climate*, 30(8), 2717–2737. <https://doi.org/10.1175/jcli-d-16-0605.1>
- Persson, P. O. G., Shupe, M. D., Perovich, D., & Solomon, A. (2017). Linking atmospheric synoptic transport, cloud phase, surface energy fluxes, and sea-ice growth: Observations of midwinter Sheba conditions. *Climate Dynamics*, 49(4), 1341–1364. <https://doi.org/10.1007/s00382-016-3383-1>
- Pithan, F., Svensson, G., Caballero, R., Chechin, D., Cronin, T. W., Ekman, A. M., et al. (2018). Role of air-mass transformations in exchange between the Arctic and mid-latitudes. *Nature Geoscience*, 11(11), 805–812. <https://doi.org/10.1038/s41561-018-0234-1>
- Pond, S., Fissel, D., & Paulson, C. (1974). A note on bulk aerodynamic coefficients for sensible heat and moisture fluxes. *Boundary-Layer Meteorology*, 6(1–2), 333–339. <https://doi.org/10.1007/bf00232493>
- Renfrew, I. A., Barrell, C., Elvidge, A., Brooke, J., Duscha, C., King, J., et al. (2021). An evaluation of surface meteorology and fluxes over the Iceland and Greenland Seas in ERA5 reanalysis: The impact of sea ice distribution. *Quarterly Journal of the Royal Meteorological Society*, 147(734), 691–712. <https://doi.org/10.1002/qj.3941>
- Rudels, B., Korhonen, M., Budéus, G., Beszczynska-Möller, A., Schauer, U., Nummelin, A., et al. (2012). The East Greenland Current and its impacts on the Nordic Seas: Observed trends in the past decade. *ICES Journal of Marine Science*, 69(5), 841–851. <https://doi.org/10.1093/icesjms/fss079>
- Schyberg, H., Yang, X., Køltzow, M., Amstrup, B., Bakketun, Å., Bazile, E., et al. (2020a). Arctic regional reanalysis on pressure levels from 1991 to present [Dataset]. *CDS*. <https://cds.climate.copernicus.eu/datasets/reanalysis-carra-pressure-levels?tab=overview>
- Schyberg, H., Yang, X., Køltzow, M., Amstrup, B., Bakketun, Å., Bazile, E., et al. (2020b). Arctic regional reanalysis on single levels from 1991 to present [Dataset]. *CDS*. <https://cds.climate.copernicus.eu/cdsapp#!/dataset/reanalysis-carra-single-levels?tab=overview>
- Screen, J. A., & Simmonds, I. (2010). Increasing fall-winter energy loss from the arctic ocean and its role in arctic temperature amplification. *Geophysical Research Letters*, 37(16), L16707. <https://doi.org/10.1029/2010gl044136>
- Strong, C., Foster, D., Cherkaev, E., Eisenman, I., & Golden, K. M. (2017). On the definition of marginal ice zone width. *Journal of Atmospheric and Oceanic Technology*, 34(7), 1565–1584. <https://doi.org/10.1175/jtech-d-16-0171.1>
- Taylor, P. C., Hegyi, B. M., Boeke, R. C., & Boisvert, L. N. (2018). On the increasing importance of air-sea exchanges in a thawing Arctic: A review. *Atmosphere*, 9(2), 41. <https://doi.org/10.3390/atmos9020041>
- Terpstra, A., Renfrew, I. A., & Sergeev, D. E. (2021). Characteristics of cold-air outbreak events and associated polar mesoscale cyclogenesis over the North Atlantic region. *Journal of Climate*, 34(11), 4567–4584. <https://doi.org/10.1175/JCLI-D-20-0595.1>
- Tsukernik, M., Kindig, D. N., & Serreze, M. C. (2007). Characteristics of winter cyclone activity in the northern North Atlantic: Insights from observations and regional modeling. *Journal of Geophysical Research*, 112(D3), D03101. <https://doi.org/10.1029/2006jd007184>
- Urbaniński, J. A., & Litwicka, D. (2022). The decline of Svalbard land-fast sea ice extent as a result of climate change. *Oceanologia (Wroclaw)*, 64(3), 535–545. <https://doi.org/10.1016/j.oceano.2022.03.008>
- Walbröl, A., Michaelis, J., Becker, S., Dorff, H., Ebell, K., Gorodetskaya, I., et al. (2024). Contrasting extremely warm and long-lasting cold air anomalies in the north Atlantic sector of the arctic during the HALO-(AC)3 campaign. *Atmospheric Chemistry and Physics*, 24(13), 8007–8029. <https://doi.org/10.5194/acp-24-8007-2024>
- Wang, C., Graham, R. M., Wang, K., Gerland, S., & Granskog, M. A. (2019). Comparison of ERA5 and ERA-interim near-surface air temperature, snowfall and precipitation over Arctic sea ice: Effects on sea ice thermodynamics and evolution. *The Cryosphere*, 13(6), 1661–1679. <https://doi.org/10.5194/tc-13-1661-2019>

- Wickström, S., Jonassen, M., Vihma, T., & Uotila, P. (2020). Trends in cyclones in the high-latitude North Atlantic during 1979–2016. *Quarterly Journal of the Royal Meteorological Society*, *146*(727), 762–779. <https://doi.org/10.1002/qj.3707>
- Wu, P., Ovchinnikov, M., Xiao, H., Lackner, C. P., Geerts, B., Tornow, F., & Elsaesser, G. (2025). Effect of ice number concentration on the evolution of boundary layer clouds during arctic marine cold-air outbreaks. *Journal of Geophysical Research: Atmospheres*, *130*(3), e2024JD041282. <https://doi.org/10.1029/2024jd041282>
- Yang, X., Schyberg, H., Palmason, B., Bojarova, J., Box, J., Pagh Nielsen, K., et al. (2020). C3S Arctic regional reanalysis—Full system documentation. Retrieved from <https://climate.copernicus.eu/copernicus-arctic-regional-reanalysis-service>
- Yu, L., Zhang, Z., Zhou, M., Zhong, S., Lenschow, D. H., Li, B., et al. (2013). Trends in latent and sensible heat fluxes over the oceans surrounding the Arctic Ocean. *Journal of Applied Remote Sensing*, *7*(1), 073531. <https://doi.org/10.1117/1.jrs.7.073531>
- Zängl, G., & Hoinka, K. P. (2001). The tropopause in the Polar Regions. *Journal of Climate*, *14*(14), 3117–3139. [https://doi.org/10.1175/1520-0442\(2001\)014<3117:ttitpr>2.0.co;2](https://doi.org/10.1175/1520-0442(2001)014<3117:ttitpr>2.0.co;2)
- Zheng, X., Zhang, Y., Klein, S., Zhang, M., Zhang, Z., Deng, M., et al. (2024). Using satellite and arm observations to evaluate cold air outbreak cloud transitions in E3SM global storm-resolving simulations. *Geophysical Research Letters*, *51*(8), e2024GL109175. <https://doi.org/10.1029/2024gl109175>